13 July 2026

# How the Oxidation State Drives Bonding Properties in CeIII and CeIV Tris(amidinate) Complexes

Emily M. Reynolds[1], Nicolas Günther-Schmidt[2], Ralph Steininger[3], Cedric Y. Reitz[1], Jörg Göttlicher[3], Constantin Wansorra[3,4], Mary Blankenship[3,5,4], Jacob A. Branson[1], Xiaofei Sun[2], Bianca Schacherl[1], Cristian Celis-Barros[6], Dirk Hauschild[3,5,4], Clemens Heske[3,4,5], Lothar Weinhardt[3,4,5], Harry Ramanantoanina[1], Peter W. Roesky[2,7], Tonya Vitova[1]

1. Institute for Nuclear Waste Disposal (INE), Karlsruhe Institute of Technology (KIT)
2. Institute for Inorganic Chemistry (AOC), Karlsruhe Institute of Technology (KIT)
3. Institute for Photon Science and Synchrotron Radiation (IPS), Karlsruhe Institute of Technology (KIT)
4. Department of Chemistry and Biochemistry, University of Nevada, Las Vegas (UNLV)
5. Institute for Chemical Technology and Polymer Chemistry (ITCP), Karlsruhe Institute of Technology (KIT)
6. Radioisotope Science and Technology Division, Oak Ridge National Laboratory
7. Institute of Nanotechnology (INT), Karlsruhe Institute of Technology (KIT)

## Abstract

We report the synthesis and characterization of a pair of homoleptic cerium tris(amidinate) complexes, $[Ce^{III}\{PhC(N^tBu)_2\}_3]$ and $[Ce^{IV}\{PhC(N^tBu)_2\}_3][Al(OC_4F_9)_4]$, containing cerium in both its trivalent ($Ce^{III}$) and tetravalent ($Ce^{IV}$) oxidation states. To the best of our knowledge, these represent the first examples of a lanthanide-amidinate system where both trivalent and tetravalent complexes have been isolated and structurally characterized in such a congruent ligand coordination. With electronic structure and bond analysis, we demonstrate that while the metal-ligand bonding in both species is dominated by interactions involving Ce 5d valence orbitals, there is a measurable participation of the 4f orbitals specifically within the $Ce^{IV}$ homolog. Ce $L_3$-edge high-energy resolution X-ray absorption near edge structure (HR-XANES) and valence band resonant inelastic X-ray scattering (VB-RIXS) are employed to evaluate the bonding properties and are complemented with quantum chemical calculations based on density-functional theory (DFT). Crucially, the high-resolution nature of these spectroscopic techniques, coupled with theoretical modelling, enables a quantitative deconvolution of the bonding interaction directly from the experimental data. This approach allows us to partition the individual contributions of both the 4f and 5d electrons to the metal-ligand interaction. Our findings highlight the increased role of 4f electron density

Posted on 13 July 2026 — CC-BY-NC-ND 4.0 — This is a preprint and has not been peer reviewed. Data may be preliminary. — https://doi.org/10.26434/chemrxiv.15006000/v1

in stabilizing high-valent lanthanide complexes, due to improved energetic and spatial overlap between nitrogen donor lone pairs and the $Ce^{IV}$ acceptor manifold.

Posted on 13 July 2026 — CC-BY-NC-ND 4.0 — This is a preprint and has not been peer reviewed. Data may be preliminary. — https://doi.org/10.26434/chemrxiv.15006000/v1

# How the Oxidation State Drives Bonding Properties in $Ce^{III}$ and $Ce^{IV}$ Tris(amidinate) Complexes

Emily M. Reynolds[†], Nicolas Günther-Schmidt[#], Ralph Steininger[§], Cedric Y. Reitz[†], Jörg Göttlicher[§], Constantin Wansorra[§+], Mary Blankenship[§+%], Jacob A. Branson[†], Xiaofei Sun[#], Bianca Schacherl[†], Cristian Celis-Barros[°], Dirk Hauschild[§+%], Clemens Heske[§+%], Lothar Weinhardt[§+%*], Harry Ramanantoanina[†], Peter W. Roesky[#^*], Tonya Vitova[†*]

[†]Institute for Nuclear Waste Disposal (INE), Karlsruhe Institute of Technology (KIT), Karlsruhe, Germany; [#]Institute for Inorganic Chemistry (AOC), KIT, Karlsruhe, Germany; [§]Institute for Photon Science and Synchrotron Radiation (IPS), KIT, Karlsruhe, Germany; [+]Department of Chemistry and Biochemistry, University of Nevada, Las Vegas (UNLV), Las Vegas, USA; [%]Institute for Chemical Technology and Polymer Chemistry (ITCP), KIT, Karlsruhe, Germany; [°]Radioisotope Science and Technology Division, Oak Ridge National Laboratory, Oak Ridge, USA; [^] Institute of Nanotechnology (INT), KIT, Karlsruhe, Germany

*corresponding authors

**ABSTRACT:** We report the synthesis and characterization of a pair of homoleptic cerium tris(amidinate) complexes, $[Ce^{III}\{PhC(N^tBu)_2\}_3]$ and $[Ce^{IV}\{PhC(N^tBu)_2\}_3][Al(OC_4F_9)_4]$, containing cerium in both its trivalent ($Ce^{III}$) and tetravalent ($Ce^{IV}$) oxidation states. To the best of our knowledge, these represent the first examples of a lanthanide-amidinate system where both trivalent and tetravalent complexes have been isolated and structurally characterized in such a congruent ligand coordination. With electronic structure and bond analysis, we demonstrate that while the metal-ligand bonding in both species is dominated by interactions involving Ce *5d* valence orbitals, there is a measurable participation of the *4f* orbitals specifically within the $Ce^{IV}$ homolog. Ce $L_3$-edge high-energy resolution X-ray absorption near edge structure (HR-XANES) and valence band resonant inelastic X-ray scattering (VB-RIXS) are employed to evaluate the bonding properties and are complemented with quantum chemical calculations based on density-functional theory (DFT). Crucially, the high-resolution nature of these spectroscopic techniques, coupled with theoretical modelling, enables a quantitative deconvolution of the bonding interaction directly from the experimental data. This approach allows us to partition the individual contributions of both the *4f* and *5d* electrons to the metal-ligand interaction. Our findings highlight the increased role of 4f electron density in stabilizing high-valent lanthanide complexes, due to improved energetic and spatial overlap between nitrogen donor lone pairs and the $Ce^{IV}$ acceptor manifold.

## INTRODUCTION

Understanding the nature of the chemical bond remains a challenging goal in chemistry, tracing its origin back to the pioneering work of Lewis,[1] whose theory of electron-pair sharing emphasized the importance of bond covalency in predicting the reactivity and properties of chemical species. In this sense, bond covalency is traditionally understood as an aggregation of electron density between two nuclei in the form of sharing an electron (pair).[2] In coordination chemistry, covalency plays an important role, as the degree of orbital mixing between metal and ligand directly influence electronic structure, most easily visible in the application of molecular orbital theory.[3] Covalency is not traditionally understood to contribute to lanthanide (Ln) bonding.[4, 5] In contrast, it is generally understood that the lanthanide elements form largely ionic bonds due to their core-like *4f* orbitals, while their heavier actinide analogues can participate in covalent bonding involving the more diffuse *5f* orbitals, though not as extensively as the *d*-block elements.[4, 5] Some studies have called that understanding into question, with tetravalent cerium being an object of particular interest, in part due to its abundant application, e.g., in automotive catalysis[6],and unique physical properties, such as *4f* covalency and hybridization of *4f* states, resulting in effects like temperature-independent paramagnetism and intense color.[7-9, 10] However, covalent contributions to bonding have been reported in a number of publications involving other lanthanide species in +II,[11] +III,[12, 13] +IV,[8, 14] and +V[15] oxidation states. Bond covalency can be described by the degree of mixing between metal and ligand valence orbitals. This mixing increases with stronger orbital overlap and/or a smaller energy separation between them.[4] Thereby, both the formal oxidation state of the metal atom and the makeup of the ligand coordination will play a role in the contribution of covalency to bonding, though the two influences are difficult to separate.[16]

One of the most controversial discussions has concerned the electronic structure and bonding of cerocene ($Ce(\eta^8\text{-}C_8H_8)_2$),[17-19] with a large body of work involving Ce $L_3$-edge high-energy-resolution X-ray absorption near-edge structure (HR-XANES), Ce $M_{4,5}$-edge and C K-edge XANES, and accompanying theoretical calculations. This has shaped the way we understand its electronic structure, the discussion which has moved from controversy regarding the formal Ce

oxidation state[20] to the more recent interpretation featuring a multiconfigurational ground state of Ce and covalent mixing of Ce *4f* orbitals with ligand C *2p* orbitals.[17-19, 21] A possible explanation for cerocene's unique properties lies in the energetic positions of the Ce *5d* and *4f* orbitals and the way atoms in stable compounds distribute electron density in order to avoid a large charge on a single atom of the molecule, as described in Pauling's electroneutrality principle.[19, 22] The unique cerocene spectrum indicates that, instead of utilizing covalency to reduce net charge, the Ce in cerocene takes on a multiconfigurational ground state with a high contribution of the $Ce^{III}$ to the wavefunction.[19] A compound with an isoelectric ligand, bis(permethylpentalene) cerium ($Ce(\eta^8\text{-}C_8Me_6)_2$), has also shown evidence of a multiconfigurational ground state and a self-contained Kondo-effect,[23] which describes the formation of a magnetic singlet via polarization of conduction electrons by a local magnetic moment, and is an effect that has also garnered interest in cerocene.[24] Literature suggests that the multiconfigurational ground state does not occur in all (formally) $Ce^{IV}$ compounds, with an alternative explanation involving ligand to metal donation bonding reported for example for $CeO_2$[17] and hexahalide $Ce^{IV}$ complexes.[7]

A more limited body of research is available on the bonding properties of $Ce^{IV}$ compounds involving sigma donations from nitrogen lone pairs, in contrast to an aromatic system with delocalized electrons that interact directly with the central atom. Evidence suggests that such N-donor ligands do not tend toward a multiconfigurational ground state and the spectra can instead be modelled with a single ground state with *4f*/*5d* mixing in the bonding interactions.[25] Moreau et al. found a notable difference in the covalent behavior of when comparing Ce–imido and Ce–oxo bonds in Ce(IV) complexes supported by a tris(hydroxylaminato) ligand, with the oxo complexes showing evidence of a higher level of ionicity.[25] When looking into $Ce^{IV}$-N coordinating complexes, Ce $L_3$-edge XANES has been used to study a variety of bonding motifs and gain varied insight into their electronic structure and other bonding properties.[10, 26]

Our work aims to provide insight into the influence of the formal $Ce^{IV}$ oxidation state when compared to a $Ce^{III}$ homologue. This comparison will bridge a gap in the fundamental understanding of how Ce in these two oxidation states forms chemical bonds and the role of covalency in the chemical bonds of Ce, N, and donor ligands.

We focus on characterizing differences in the Ce *4f* and *5d* contributions to covalent bonding interactions in isostructural $Ce^{III}$ and $Ce^{IV}$ complexes with N-donor ligands. Amidinate ligands provide a versatile platform for stabilizing cerium in formal oxidation states of +III and +IV and are therefore well-suited for probing bonding trends in *f*-element chemistry. Previous studies on tetravalent cerium amidinate complexes have predominantly addressed neutral complexes, in which changes to formal oxidation state were accompanied by coordination environment variation compared to their trivalent analogues.[27]

We designed amidinate-based cerium complexes and successfully isolated a cationic $Ce^{IV}$-amidinate complex stabilized by a weakly coordinating anion (WCA), $[Al(OC(CF_3)_3)_4]^-$. The same ligand framework is preserved around the metal center both for the trivalent complex $[Ce^{III}\{PhC(N^tBu)_2\}_3]$ (Ph = $[C_6H_5]^-$; $^t$Bu = $[C(CH_3)_3]^-$) and its tetravalent, cationic counterpart $[Ce^{IV}\{PhC(N^tBu)_2\}_3][Al(OC_4F_9)_4]$. The bonding properties and covalent contributions to metal–ligand bonding in this pair of analogous cerium complexes are assessed using state-of-the-art X-ray spectroscopic methods: Ce $L_3$-edge HR-XANES, resonant inelastic X-ray scattering (RIXS), and valence-band RIXS (VB-RIXS), supported by quantum chemical calculations. The homoleptic ligand coordination enables the influence of the formal Ce oxidation state on bonding to be investigated directly. In particular, Ce $L_3$-edge HR-XANES provides a powerful probe of the overall electronic structure and bonding situation in lanthanide compounds, while VB-RIXS allows the contribution of Ce 5d electron density to the metal–ligand bond to be evaluated through the analysis of peak energies and intensities associated with occupied valence orbitals. This analytical approach has previously been used to assess 5d electron-density participation in bonding in a lanthanum-based intermetallic complex,[11] and its application here enables the first direct quantitative comparison of Ce 5d participation in bonding between isostructural $Ce^{III}$ and $Ce^{IV}$ compounds.

## RESULTS AND DISCUSSION

**Synthesis and Structural Analysis.** $[Ce^{III}\{PhC(N^tBu)_2\}_3]$ was obtained by salt metathesis between three equivalents of $Li(^tBuN)_2CPh$[28] with $[Ce(BH_4)_3(thf)_3]$[29] (thf = tetrahydrofurane, $C_4H_8O$) in 80% yield (Scheme 1) and was characterized using standard analytic/spectroscopic techniques. The $^1$H NMR spectrum of $[Ce^{III}\{PhC(N^tBu)_2\}_3]$ showed paramagnetic shifts of the phenyl protons towards higher frequencies, while the tert-butyl protons exhibited a singlet signal at -2.81 ppm. Redoxreaction of $[Ce^{III}\{PhC(N^tBu)_2\}_3]$ with one equivalent of $[Ag(dcm)][Al(OC(CF_3)_3)_4]$[30] (dcm = dichloromethane) afforded $[Ce^{IV}\{PhC(N^tBu)_2\}_3][Al(OC_4F_9)_4]$ as dark blue crystalline material in 68 % yield. The $^1$H-NMR spectrum of $[Ce^{IV}\{PhC(N^tBu)_2\}_3][Al(OC_4F_9)_4]$, which was also characterized, is well resolved. The synthesis and characterization of the analogous compounds, which have methyl groups instead of phenyl groups in the amidinate backbone, $[Ce^{III}\{MeC(N^tBu)_2\}_3]$ and its tetravalent, cationic counterpart $[Ce^{IV}\{MeC(N^tBu)_2\}_3][Al(OC_4F_9)_4]$, can be found in the Supporting Information (SI).

The molecular structures of $[Ce^{III}\{PhC(N^tBu)_2\}_3]$ and $[Ce^{IV}\{PhC(N^tBu)_2\}_3][Al(OC_4F_9)_4]$ are depicted in Figure 1 and selected metrical parameters are summarized in Table S2 in the SI. Both compounds crystalize in the triclinic space group *P*-1. In each case, one molecule is present in the asymmetric unit; however, the crystal structure of $[Ce^{IV}\{PhC(N^tBu)_2\}_3][Al(OC_4F_9)_4]$ contains one molecule of non-coordinating diethyl ether besides the cationic and anionic complexes.

In both cerium complexes, the three $\eta^2$-coordinated amidinate ligands are arranged in a propeller-like fashion around the metal center, resulting in an approximately $C_3$-symmetric coordination environment. The presence of this $C_3$-screw axis results in the chiral nature of both molecules. However, as seen from the centrosymmetric space group, both compounds crystallized as a racemic mixture. The average Ce–N bond length in $[Ce^{III}\{PhC(N^tBu)_2\}_3]$ is 2.512 Å (range 2.539(2) to 2.484(2) Å), whereas a shorter average distance of 2.390 Å (range 2.365(4) to 2.409(4) Å) was observed for $[Ce^{IV}\{PhC(N^tBu)_2\}_3][Al(OC_4F_9)_4]$ (cf. SI, Table S2).

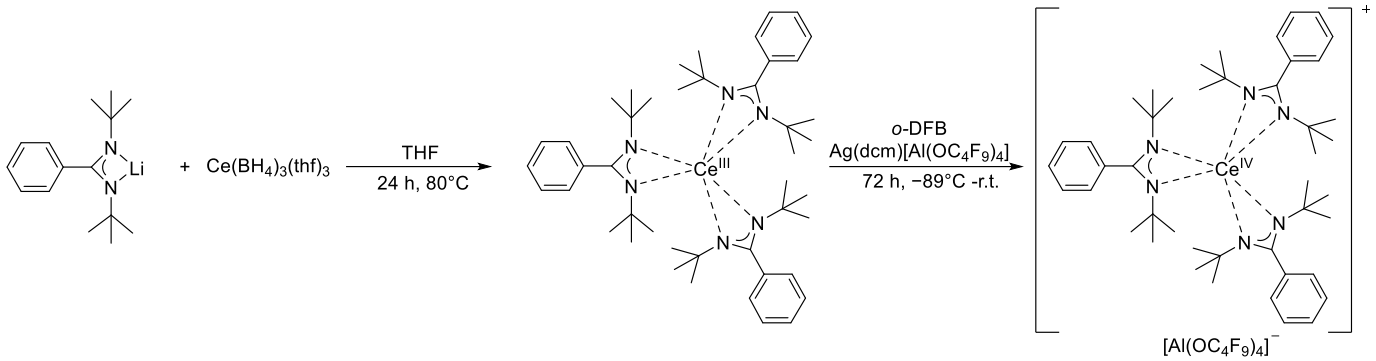


**Scheme 1.** Synthesis of $[Ce^{III}\{PhC(N^tBu)_2\}_3]$ and its tetravalent, cationic counterpart $[Ce^{IV}\{PhC(N^tBu)_2\}_3][Al(OC_4F_9)_4]$ (*o*-DFB =1,2-difluorobenzene).

This contraction is attributed to the change in formal oxidation state from $Ce^{III}$ to $Ce^{IV}$. The average decrease of 0.123 Å is in good agreement with the change in the effective ionic radii reported by Shannon for cerium at a coordination number of six (Δr ≈ 0.14 Å).[31] The average N–Ce–N bite angle is 52.74° for $[Ce^{III}\{PhC(N^tBu)_2\}_3]$ and 55.75° for $[Ce^{IV}\{PhC(N^tBu)_2\}_3][Al(OC_4F_9)_4]$, which also agrees with the differences of the bond lengths.[32]

The torsion angles of the amidinate ligands relative to the coordination plane are very similar for both complexes, averaging 56.1° for $[Ce^{III}\{PhC(N^tBu)_2\}_3]$ and 55.1° for $[Ce^{IV}\{PhC(N^tBu)_2\}_3][Al(OC_4F_9)_4]$, indicating only minor differences in ligand orientation.

UV-Vis absorption spectra of $[Ce^{III}\{PhC(N^tBu)_2\}_3]$ and $[Ce^{IV}\{PhC(N^tBu)_2\}_3][Al(OC_4F_9)_4]$ were recorded in THF at 1.12 mM and 0.56 mM respectively (Figure 2, (a)). $[Ce^{III}\{PhC(N^tBu)_2\}_3]$ displays intense UV bands at λ(max) = ~255 and ~307 nm, accompanied only by a weaker signal at 424 nm. In contrast, oxidation to $[Ce^{IV}\{PhC(N^tBu)_2\}_3][Al(OC_4F_9)_4]$ leads to markedly stronger UV absorption, despite the twofold lower concentration. The positions of the maxima do not change significantly, with λ(max) = ~257 and ~305 nm. Importantly, $[Ce^{IV}\{PhC(N^tBu)_2\}_3][Al(OC_4F_9)_4]$ exhibits a broad visible absorption centered at ~667 nm, consistent with the pronounced dark blue color of the solution, indicating an enhanced charge-transfer contribution.

Cyclic voltammetry was employed as a complementary analytical technique to confirm the accessibility of the $Ce^{IV}$ oxidation state. Measurements were performed in THF using 0.05 M $Bu_4NPF_6$ as the supporting electrolyte and a 5 mM solution of $[Ce^{III}\{PhC(N^tBu)_2\}_3]$, with an $Ag/AgNO_3$ reference electrode (10 mM $AgNO_3$ in MeCN, 0.1 M $Bu_4NPF_6$). The voltammograms display a distinct oxidative response attributed to the $Ce^{III}/Ce^{IV}$ redox couple (Figure 2, (b), and Figure S18). The observation of this electrochemical oxidation is consistent with the chemical oxidation of the complex $[Ce^{IV}\{PhC(N^tBu)_2\}_3][Al(OC_4F_9)_4]$ synthetically prepared by using $[Ag(dcm)][Al(OC(CF_3)_3)_4]$ as an oxidizing reagent. The formal redox potential was estimated from the midpoint of the anodic and cathodic peak potentials at low scan rates, yielding a value of approximately +0.05 V vs. $Ag/AgNO_3$. While the redox potential exhibits quasi-reversible behavior with increasing peak separation at higher scan rates, the electrochemical data unambiguously demonstrates that oxidation from $Ce^{III}$ to $Ce^{IV}$ is readily accessible under the applied conditions (see also Figure S19).

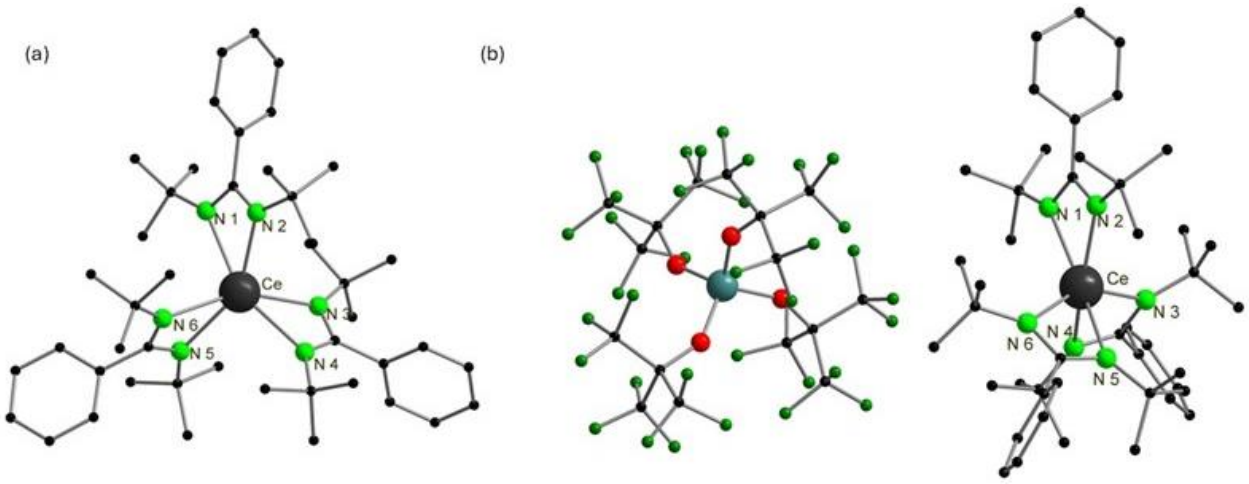


**Figure 1.** Molecular structures of (a) $[Ce^{III}\{PhC(N^tBu)_2\}_3]$ and (b) $[Ce^{IV}\{PhC(N^tBu)_2\}_3][Al(OC_4F_9)_4]$ in the solid state. For both structures, hydrogen atoms were omitted for better clarity. For $[Ce^{IV}\{PhC(N^tBu)_2\}_3][Al(OC_4F_9)_4]$, the disorder of three $OC_4F_9$-groups and one diethyl ether molecule are also omitted. Selected bond lengths and angles can be found in the SI, Table S2.

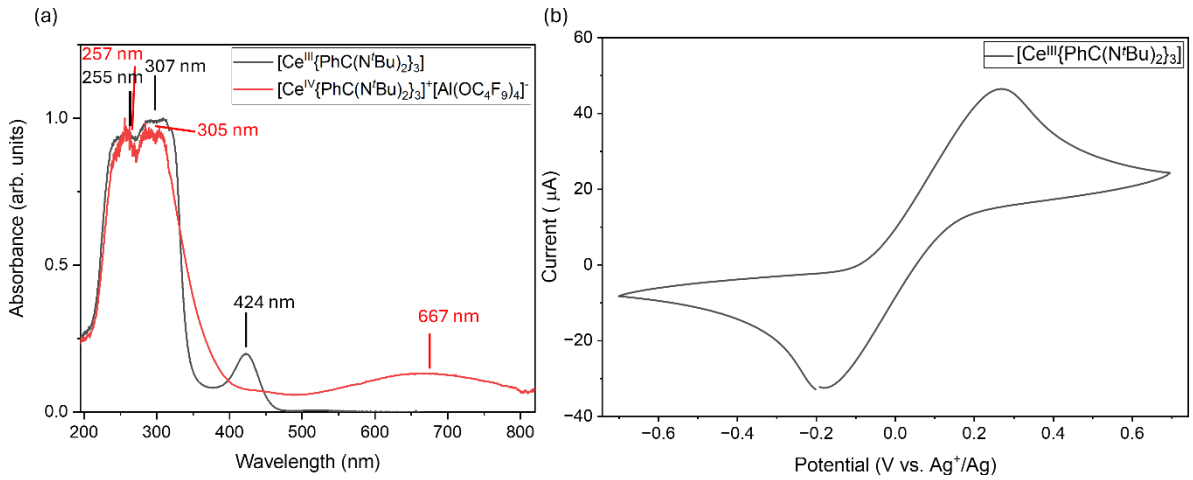


**Figure 2.** (a) UV-Vis Spectrum of $[Ce^{III}\{PhC(N^tBu)_2\}_3]$ in a 1.12 mM THF-solution and $[Ce^{IV}\{PhC(N^tBu)_2\}_3][Al(OC_4F_9)_4]$ in a 0.55 mM THF-solution recorded at room temperature. The THF contribution was subtracted. (b) Cyclovoltammetry of $[Ce^{III}\{PhC(N^tBu)_2\}_3]$ recorded in THF containing 0.05 M $Bu_4NPF_6$ at 100 mV/s. Measurements were performed using a 5 mM solution of $[Ce^{III}\{PhC(N^tBu)_2\}_3]$ with a $Ag/AgNO_3$ reference electrode (10 mM $AgNO_3$ in MeCN, 0.1 M $TBAPF_6$). The anodic wave corresponds to oxidation of $[Ce^{III}\{PhC(N^tBu)_2\}_3]$ to its tetravalent form.

**Ce $L_3$ HR-XANES.** HR-XANES of Ce at the $L_3$-edge has been used to probe the electronic structure and bonding of Ce compounds. Due to its complex shape, the Ce $L_3$-edge HR-XANES spectrum of $CeO_2$, an air and irradiation stable $Ce^{IV}$ reference, has been the object of multiple studies working towards an understanding and interpretation of its features, in particular its doubled white line (WL), the most intense structure following the absorption edge.[17, 33, 34] In order to facilitate a better understanding of the spectra of our amidinate complexes, we will shortly discuss the spectrum of $CeO_2$ here. Figure 3 (a) depicts a schematic view of the prevailing electronic transitions involved in Ce $L_3$-edge HR-XANES/VB-RIXS as well as Ce $M_{4,5}$-edge XANES, the fluorescence (emission) that results from a specific relaxation of electrons from an upper electronic level into the core-hole in a lower level is monitored as a function of excitation energy across the absorption edge. This results in a spectrum that is essentially a cut through a RIXS map at the chosen emission energy. At the Ce $L_3$-edge, electrons are predominantly excited from the Ce $2p_{3/2}$ orbital into unoccupied *5d*-dominated molecular orbitals (Figure 3, (a)), following the dipole selection rules for the electronic transitions ($\Delta l=\pm1$, $\Delta j=0, \pm1$). This determines the intermediate state $2p^1{}_{3/2}\,5d^1$ of the RIXS process while the final state $3d^3{}_{3/2}\,5d^1$ is selected by the detected fluorescence transition. In both of these states, a core-hole is present.

In the case of $CeO_2$, a mixed valent intermediate state resulting from ligand-metal orbital mixing is present. This means that both $2p^1{}_{3/2}4f^0$ and $2p^1{}_{3/2}4f^1\underline{L}$ intermediate states play a role, in which the $2p^1{}_{3/2}4f^1\underline{L}$ intermediate state involves electron density originally stemming from the ligand (L). It has been an object of discussion whether the presence of these states is indicative of ground-state f-electron donation in bonding. Recent advances in the field indicate a direct relationship between the presence of intermediate states with 4f-ligand mixing (charge transfer from ligand to metal) and 4f-electron donation to bonding in the ground state, as the Ce $L_3$-edge spectrum of $CeO_2$ is theoretically reproducible considering a single ground state configuration (if the model assumes electron donation from the ligand to the metal, i.e. covalent bonding interaction in the ground state).[17] It can also be described by assuming a mixed-valence ground state, which involves hybridized $4f^0$ and $4f^1\underline{L}$ ground states as reported in the literature,[35] though this can be transformed into the former situation and is computationally equivalent.[17] For certain cerium compounds like cerocene, the spectrum cannot be modeled by only considering covalent bonding interaction in the ground state (single ground state electron configuration), therefore the ground state is suggested to be multiconfigurational.[17] The mixed intermediate state of $CeO_2$ results in two white lines (the most intense absorption resonance): one at lower energies, corresponding to the $4f^1\underline{L}$ configuration, and one at higher energies, corresponding to the $4f^0$ configuration, which is the expected formal configuration for $Ce^{IV}$ compounds (Figure 3, (b)). The presence of more electron density in the 4f-based orbitals of the $4f^1\underline{L}$ configuration leads to increased screening of the core-hole from the viewpoint of higher-lying molecular orbitals. The resulting energetic stabilization shifts the corresponding edge feature to lower excitation energies, which in this case is visible as a separate WL in the spectrum. Therefore, the presence of a double WL in Ce $L_3$-edge spectra indicates the presence of electron donation from the ligand to Ce *4f* orbitals and, as a result, bond covalency or a multiconfigurational ground state, such as in cerocene.

When comparing the spectra of $[Ce^{III}\{PhC(N^tBu)_2\}_3]$ and $[Ce^{IV}\{PhC(N^tBu)_2\}_3][Al(OC_4F_9)_4]$ with their reference compounds $CeCl_3$ and $CeO_2$, the general spectral shapes of the WLs of the complexes match those of the reference compound with the corresponding oxidation state (Figure 4). Because details like the intensity ratio and sub-features of the $4f^1\underline{L}$ and $4f^0$ WLs are similar, the spectra suggest that the bonding situation in the $Ce^{IV}$ imine complex is similar to the bonding situation in $CeO_2$, i.e., *4f*-electron density plays a significant role in bonding in the form of ligand to metal donation in a ground state involving a single electron configuration. A shift of the absorption edge to lower energies beginning with the oxide and $[Ce^{IV}\{PhC(N^tBu)_2\}_3][Al(OC_4F_9)_4]$,

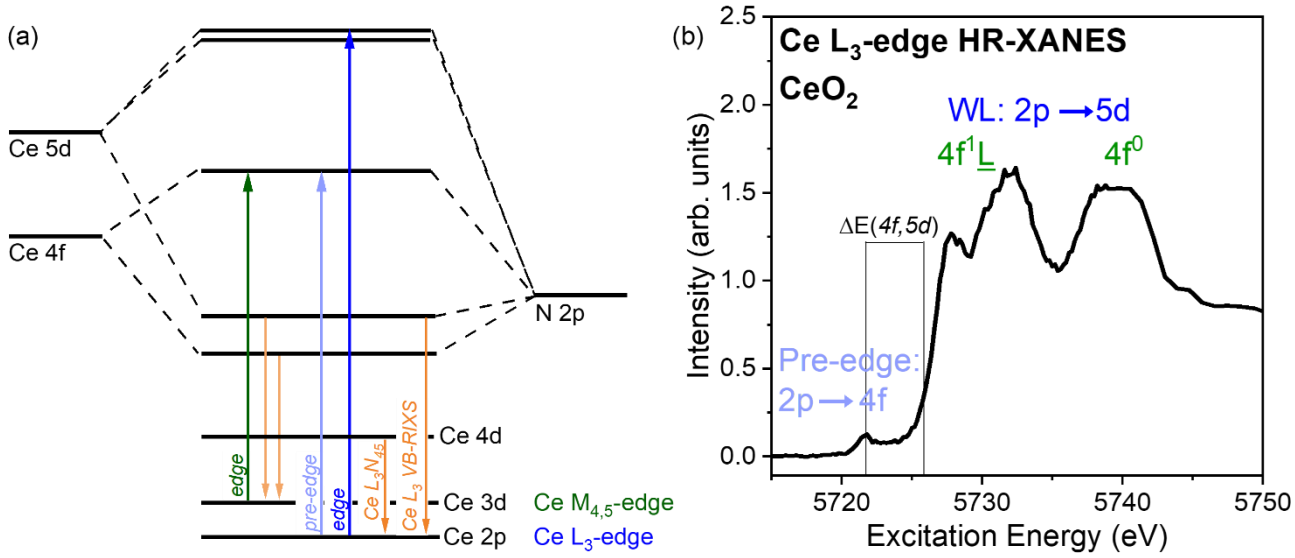


**Figure 3.**(a) A simplified, qualitative molecular orbital electron transition scheme for the X-ray absorption edges and deexcitation channels presented here and (b) cerium $L_3$-edge HR-XANES spectrum of $CeO_2$, a stable $Ce^{IV}$ reference, with features labelled with dominant transitions in blue and electron configurations in green.

followed by the chloride, and then the $[Ce^{III}\{PhC(N^tBu)_2\}_3]$, can be observed. The shift to lower excitation energies for compounds in lower nominal oxidation states is due to a higher electron density, shielding the outer electrons from the nucleus' positive charge, the effective charge of which formally increases in the presence of core-holes in the intermediate and final states of the excitation process. In the case of the $L_3$-edge spectrum, this affects both the pre-edge feature(s), resulting from transitions into *4f*-dominated molecular orbitals, and the edge-feature(s) stemming from transitions into *5d*-dominated molecular orbitals. While transitions into the 4f-dominated molecular orbitals at the pre-edge are dipole-forbidden, these can become visible due to quadrupole transitions and *4f*/*5d* mixing occurring in compounds lacking inversion symmetry, which may be the case here, and can lead to multiple pre-edge features.

In previous work, the energy difference between the pre-edge and edge features of Lanthanum $L_3$-edge HR-XANES (ΔE(*5d,4f*)) was proposed as a measure of bond covalency for trivalent compounds.[13] This energy difference reflects the natural difference in energy between the *4f* and *5d* orbitals of the free atom in a given oxidation state; it is sensitive to the effect of the spherical component of the ligand-field potential on orbital energies, and is influenced heavily by core-hole screening effects, which play a significant role in HR-XANES.[13] Due to the radial distribution of the orbitals, *4f* orbitals are more influenced by core-hole screening-effects than *5d* orbitals, leading to larger energy stabilization, and because a larger core-hole screening effect (and increased ligand-field effect) are indicators for ionic bonding interactions, a larger ΔE(*5d,4f*) value is associated with ionicity in bonding as well.[13] In contrast, a smaller value hints at increased *5d*-ligand mixing, thereby serving as an indicator for higher bond covalency.[13] We were able to validate this metric for $La^{3+}$ and assume the argumentation is valid for trivalent Ln systems. Since certain effects that play into the size of ΔE(*5d,4f*) are inseparable from the formal oxidation state of the atom, this value is best compared within groups of compounds with the same formal oxidation state,

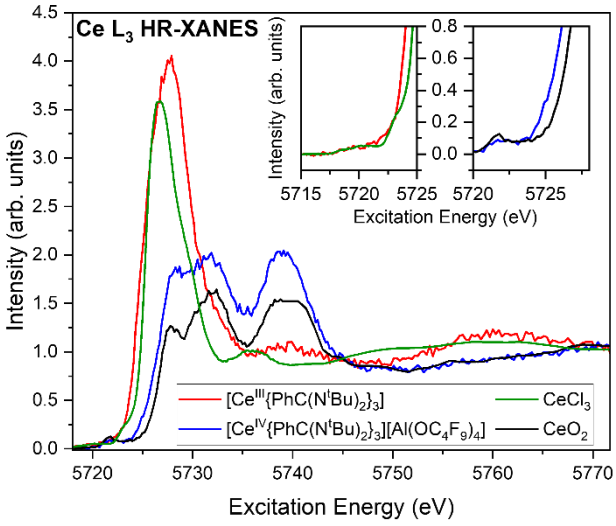


**Figure 4.** Ce $L_3$-edge HR-XANES of $[Ce^{III}\{PhC(N^tBu)_2\}_3]$ and $[Ce^{IV}\{PhC(N^tBu)_2\}_3]$ $[Al(OC_4F_9)_4)]$ and reference compounds of the same formal oxidation state, $CeCl_3$ and $CeO_2$, with direct comparisons of the pre-edge regions shown in the insets.

and use for compounds of a different oxidation state, like $Ce^{IV}$ compounds, need to be treated with caution due to increased 5d hybridization. Energy differences were estimated for all combinations of pre-edge and edges (cf. SI, Figure S22). The energy differences between pre-edge and edge are smaller for the $[Ce^{III}\{PhC(N^tBu)_2\}_3]$ than $CeCl_3$ for both pre-edges present in both spectra (4.6 eV and 2.8 eV (± 0.2 eV) for $[Ce^{III}\{PhC(N^tBu)_2\}_3]$, 6.6 eV and 5.0 eV (± 0.9 eV) for $CeCl_3$).

This indicates stronger interaction of the *5d* orbitals with ligand orbitals to form the bond, and therefore a stronger covalent interaction in the complex than in the chloride salt, which matches expectations. When comparing the energy differences in the Ce(IV) compounds, which have one singular pre-edge but two main edges as described above, we notice that both values are very similar, but the energy

difference is slightly higher for the $[Ce^{IV}\{PhC(N^tBu)_2\}_3][Al(OC_4F_9)_4]$ complex than for $CeO_2$, though this difference is more prominent for the expected $4f^0$ peak than the second peak from the charge transfer induced $4f^1\underline{L}$ ground state (the values being 5.2 eV and 15.8 eV for $[Ce^{IV}\{PhC(N^tBu)_2\}_3][Al(OC_4F_9)_4]$ and 5.0 eV and 15.4 eV for $CeO_2$). Because the values are so similar and the metric needs to be treated with caution in $Ce^{IV}$ compounds, this result does not indicate differences in covalency. In total, the observation of the pre-edge energy differences in combination with the spectral features indicate that the Ce-ligand bond in $CeCl_3$ is least covalent, followed by the $Ce^{III}$ Trisamidinate], and the $Ce^{IV}$ Trisamidinate and $CeO_2$ being similarly covalent. It is interesting to note here, that these spectra were taken recording the $L_3N_{45}$ emission line rather than the $L_3M_5$ emission line, which has been shown to result in pre-edges and edges that are closer in energy to each other, as well as slight differences in spectral features.[36]

Another easy-to-notice difference in the spectra of the cerium compounds is the position of the first oscillation in the post-edge. Often, a post-edge that is shifted to lower energies is a result of longer bond lengths in the first coordination shell. Because this resonance is shifted to lower energies for $[Ce^{III}\{PhC(N^tBu)_2\}_3]$ (average Ce-N bond length of 2.51 Å) by ca. 10 eV in comparison to $[Ce^{IV}\{PhC(N^tBu)_2\}_3][Al(OC_4F_9)_4]$ (average Ce-N bond length of 2.39 Å), supporting the experimental structure determined using X-ray crystallography (cf. SI, Section 3).

Further insight into bonding and its influences can be gained by investigating the crystal field splitting in the experimental spectra (cf. Figure S23). Interestingly, in a comparative analysis between the compounds with the formal oxidation state +IV, the crystal field splitting of $CeO_2$ is larger than that of $[Ce^{IV}\{PhC(N^tBu)_2\}_3][Al(OC_4F_9)_4]$. This is likely an effect of the change in geometry from cubic with eight-fold square prismatic coordination[37] to a distorted octahedral coordination with six N atoms (cf. SI, Figures S14 and S15), as well as a possible effect of increased electron density on the central atom.

**Ce $L_3$-edge VB-RIXS.** In order to study the character of the bonds from the perspective of the valence orbitals, Ce $L_3$-edge VB-RIXS was employed (Figure 5). VB-RIXS spectra were measured by setting the excitation energy to the maximum of the WL. For $[Ce^{III}\{PhC(N^tBu)_2\}_3]$, the excitation energy was set to 5727.8 eV. For $[Ce^{IV}\{PhC(N^tBu)_2\}_3][Al(OC_4F_9)_4]$], spectra were recorded at both the first WL (5728.4 eV) and second WL (5738.4 eV), and then scanning over the emission energy towards lower emission energies. This allows the observation of fluorescence that is energetically close to the edge, originating from electron transitions from the valence band (see inset in Figure 5). After normalization to the intensity of the 5s signal ($L_3O_1$ emission line, 5685.6 eV, see discussion below, Figure 6). We assume that the Ce 5s orbitals do not participate strongly in bonding, which makes this type of normalization feasible. Next to the elastic peak for the $[Ce^{III}\{PhC(N^tBu)_2\}_3]$ complex we find the prominent signal A.I as well as its small satellite A.II. For $[Ce^{IV}\{PhC(N^tBu)_2\}_3][Al(OC_4F_9)_4]$, the spectrum taken at the first WL excitation exhibits a prominent peak B.I and two weak features B.II and B.III.

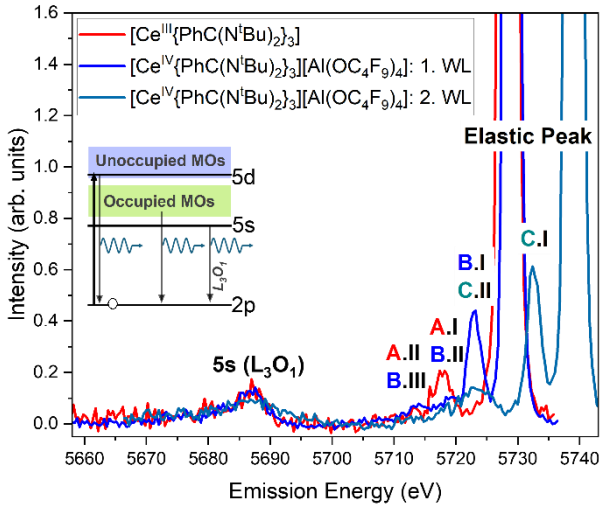


**Figure 5.** NormalizedVB-RIXS of $[Ce^{III}\{PhC(N^tBu)_2\}_3]$ ($4f^1$ configuration, A), $[Ce^{IV}\{PhC(N^tBu)_2\}_3][Al(OC_4F_9)_4]$, when excited at the 1st white line ($4f^1$, B), and excited at the 2nd white line, ($4f^0$, C) of the Ce $L_3$-edge HR-XANES (see also Figure 6, (d)). A schematic representation of the processes underlying the measurement is shown in the inset. The emission signals for each spectrum are labelled with roman numerals from highest to lowest emission energy and the signal known as the Ce $L_3O_1$ emission line is marked.

in Figure 5). After normalization to the integral intensity of the 5s signal ($L_3O_1$ emission line, 5685.6 eV, see discussion below, Figure 6), spectra were compared on the absolute energy scale (Figure 5). In contrast, the spectrum taken at the second white line (C) has two prominent features next to the elastic peak (C.I and C.II) and that C.II is at the same emission energy as B.I.

When comparing the spectra to angular momentum projected density of state (PDOS) computations performed using the Amsterdam Density Functional (ADF) code[38], the dominating contribution of final states with a 5s electron hole to the emission at ca. -35 to -55 eV is confirmed (Figure 6, (a)-(c)). The calculation also suggests that the signals close to the elastic peak are dominated by final states with a $5d$ electron hole ($5d^{-1}$).

For a more detailed discussion of the spectra of $[Ce^{IV}\{PhC(N^tBu)_2\}_3][Al(OC_4F_9)_4]$, when excited at the 1st and 2nd white line, the different intermediate and final states need to be taken into account. As discussed above, excitation at the 1st white line corresponds to a $2p^54f^1$ intermediate state. We then attribute feature B.I to a $5d^{-1}4f^1$ final state, with the $L_3O_1$ emission corresponding to a $5s^{-1}4f^1$ final state. Features B.II and B.III are less straight forward. A possible explanation for these observed features lies in the unique electronic structure of $Ce^{IV}$, which leads to a double white line in the HR-XANES and may also lead to additional intensity here. However, we note that signals B.II and B.III also increase in intensity as a function of irradiation with X-rays (cf. SI, Figure S24) and it cannot be ruled out that these signals are caused by beam induced changes. For excitation at the 2nd white line, a $2p^54f^0$ intermediate state is assumed. The $L_3O_1$ emission then corresponds to a $5s^{-1}4f^0$ final state, which only shifts slightly in emission energy and broadens as compared to excitation at the 1st white line. Likewise, feature C.II corresponds to a $5d^{-1}4f^0$ final state, only slightly shifted in *emission energy* and broadened as compared to B.I for excitation at the 1st white line. Finally, C.I is at the same

*loss energy* as B.I and thus corresponds to the same final state as B.I, i.e., $5d^{-1}4f^{1}$.

To draw conclusions about the ground state, an additional process must be regarded. Because excitation at the left peak of the first WL is at the lowest energy, it is arguable that it is most likely to have little to no secondary/multielectron excitations, while excitation at the left peak of the second WL is likely to include both excitations from the ground state into an intermediate $4f^{0}$ state and multi-electron excitations. The measured fluorescence is then likely to be a result of relaxation from several different intermediate states. In Sergentu *et al.*'s theoretical study on the electronic behavior of $CeO_2$ in both its ground and excited states, a reorganization of the population of molecular orbitals upon excitation is evident.[17] With excitation at higher energies, the amount of electron density in the binding molecular orbitals involving *4f* orbitals of cerium decreases.[17] In conclusion, we argue that, in order to have a comparable gauge on the d electron density in bonding, the excitation at the lowest energy WL maximum (spectrum B) is closest to the ground state.

Assuming little to no participation of the Ce 5s levels in boding, the occupation of the 5d levels can be estimated by comparing the intensity (area) of the valence transitions to that of the emission involving 5s. For this purpose, the respective areas were determined in the VB-RIXS spectra using least-square fits using *Fityk*[39] (as described in the SI). We derive the following area ratios between the transitions involving 5d electrons and those involving 5s as follows: 0.68±0.12 for $[Ce^{III}(PhC(N^tBu)_2)_3]$, 1.65±0.15 for $[Ce^{IV}(PhC(N^tBu)_2)_3]^+[Al(OC_4F9)_4]^-$ excited at the 1st WL, and 2.48±0.24 for $[Ce^{IV}(PhC(N^tBu)_2)_3]^+[Al(OC_4F9)_4]^-$ excited at the 2nd WL. This indicates more participation of *5d* electron density in bonding, and therefore more prominent covalent contribution to Ce-ligand bonding, for the $[Ce^{IV}\{PhC(N^tBu)_2\}_3][Al(OC_4F_9)_4]$ complex than the $[Ce^{III}\{PhC(N^tBu)_2\}_3]$ complex.

**Theoretical calculations of HR-XANES and VB-RIXS spectra.** In order to verify that the assignment of the peaks performed by comparing the experimental spectra to ground states DOS (see Figure 6), we calculated the VB-RIXS

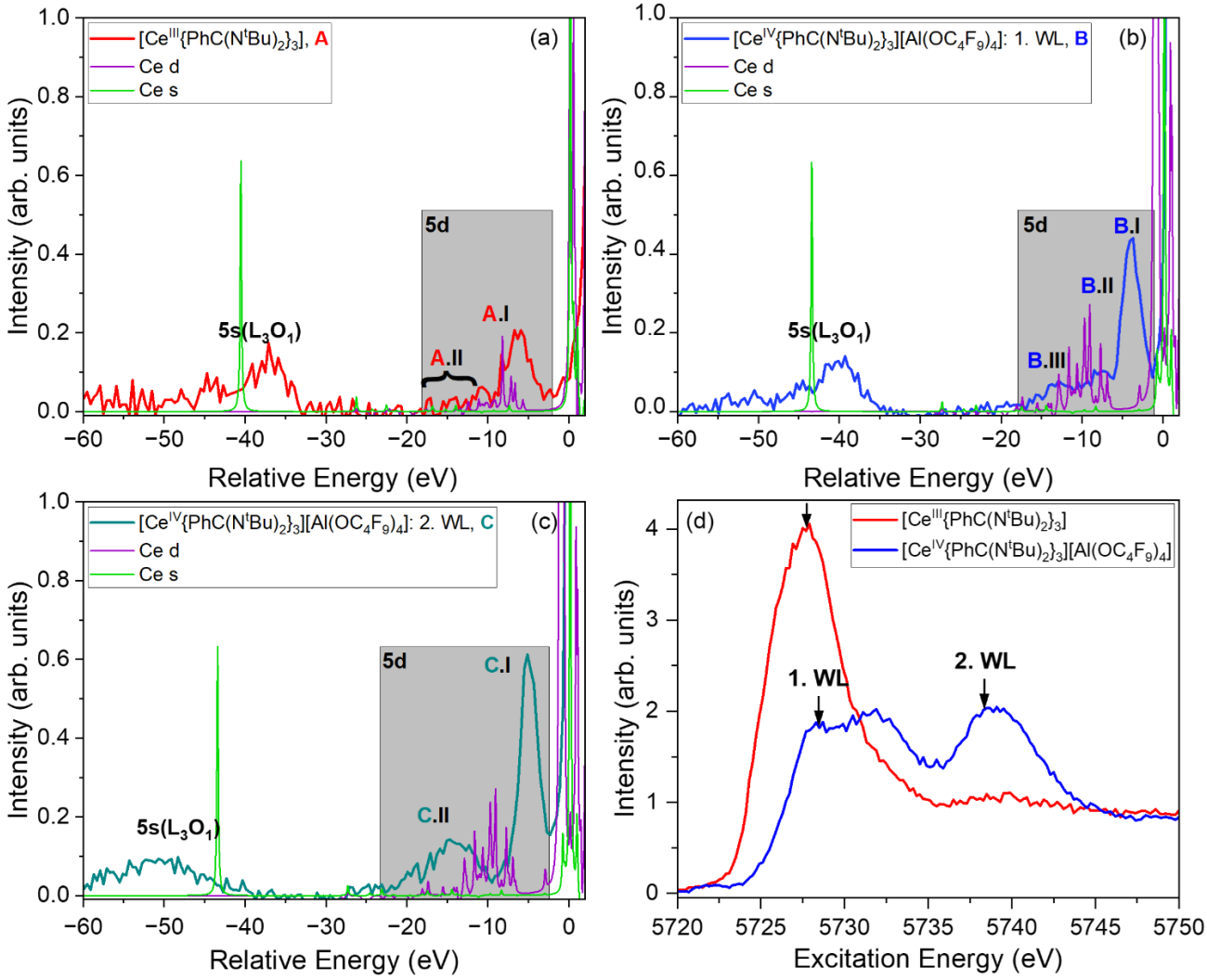


**Figure 6.** Normalized VB-RIXS spectra of (a) $[Ce^{III}\{PhC(N^tBu)_2\}_3]$ and (b) $[Ce^{IV}\{PhC(N^tBu)_2\}_3][Al(OC_4F_9)_4]$, when excited at the 1st white line or (c) the 2nd white line, compared to projected density of state calculations done with density functional theory (DFT) and Amsterdam density functional (ADF)[38] code based on theoretically optimized structures, as well as (d) HR-XANES spectra with the energies at which the excitation for the VB-RIXS took place referenced. VB-RIXS are shifted by the value of the edge of the corresponding HR-XANES.

of the Ce(III) compound using LFDFT. Figure 7 shows the Ce $L_3$-edge HR-XANES and VB-RIXS experimental spectra for $[Ce^{III}\{PhC(N^tBu)_2\}_3]$ together with the corresponding calculations used to corroborate their spectral interpretation. The theoretical VB-RIXS data is obtained by using a single-particle approximation based on TDDFT in ADF and the Kramers-Heisenberg formalism. In the XANES, we included only transitions that have GS ($2p_{3/2}^3 4f^1$) → IS ($4f^1 5d^1$) characters, allowing us to assess how the peak distribution in the absorption profiles govern the subsequent VB-RIXS decay channels. The calculated absorption spectrum shows three oscillator strengths reflecting the ligand-field splitting of the 5*d* orbitals under the local coordination environment. In $D_3$ point group, the 5*d* manifold splits into $a_1$, e and e irreducible representations. The total energy span of this splitting is calculated to be approximately 2.3 eV. However, upon broadening (to account for the core-hole lifetime broadening and instrumental energy resolution), the individual transitions merged into a broad band, which is in a good agreement with the measured HR-XANES spectrum. It should be noted that the VB-RIXS spectrum can be described using the inelastic X-ray scattering formalism. The calculated VB-RIXS map represents the GS ($2p_{3/2}^3 4f^1$) → IS ($4f^1 5d^1$) transitions, followed by the decay channel IS ($4f^1 5d^1$) → FS ($5d^1\underline{L}$). The FS corresponds to valence exciton states that result from excitation from occupied ligand-dominated orbitals with finite Ce 5*d* characters. This produces weaker inelastic scattering features at transfer energy close to 0 eV. In addition, decay channel IS ($4f^1 5d^1$) → FS ($5s^1 5d^1$) transitions are also included to reproduce the high transfer energy features that are observed in the experiment. This produces stronger inelastic scattering features at transfer energy about 50 eV. The calculated VB-RIXS spectrum is obtained as vertical cross section of the map at excitation energy that correspond to the maximum intensity of the XANES signal, and compared with the experiments. The calculated and experimental VB-RIXS data of the $[Ce^{III}\{PhC(N^tBu)_2\}_3]$ complex depicted Figure 7 are in very good agreement confirming the qualitative description for

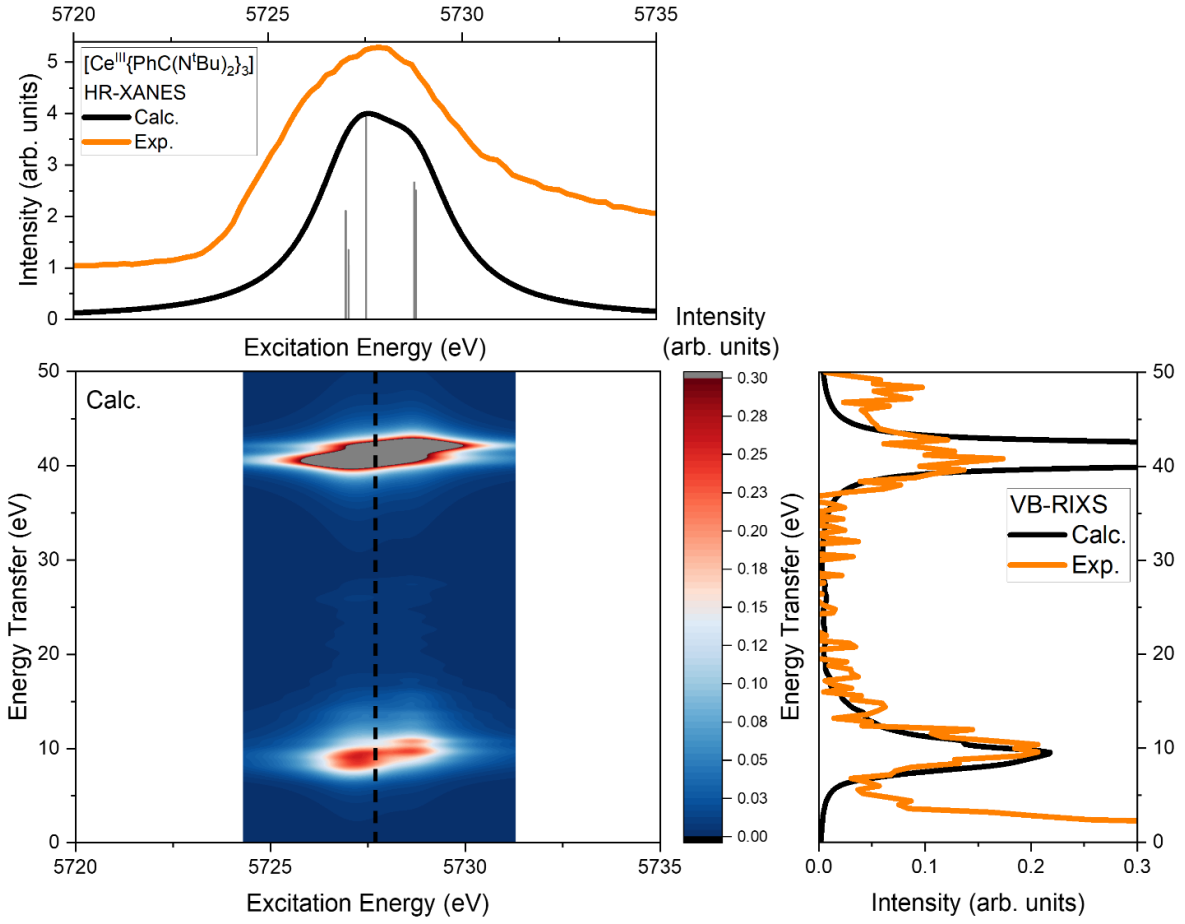


**Figure 7.** Comparison between the calculated (calc.) and experimental (exp.) Ce $L_3$-edge VB-RIXS results of $[Ce^{III}\{PhC(N^tBu)_2\}_3]$. (top) Calc. versus exp. Ce $L_3$-edge HR-XANES (black and orange traces) are presented. Calculated data is presented as oscillator strengths (gray bars) and their broadening with a Lorentzian function of HWHM = 0.80 eV (black trace); (bottom-left) calc. Ce $L_3$-edge VB-RIXS maps, obtained with the Kramers-Heisenberg formula. Solely intermediate states with $2p^5 5d^1$ electronic configuration are included, while the final state corresponds to low-lying excited states with $5d^1\underline{L}$ and $5s^1 5d^1$ electron configurations (cf. SI Theoretical Methods). Broadening of the VB-RIXS signal with a Lorentzian function of HWHM = 0.80 eV (IS) and 0.40 eV (FS); (bottom-right) calc. versus exp. Ce $L_3$-edge VB-RIXS spectra (black and orange traces). The calculated VB-RIXS spectra are obtained as vertical cuts of the VB-RIXS maps (black dashed line) at an excitation energy of 5727.7 eV. These energies correspond to the maximum of the intensity of the VB-RIXS inelastic scattering signals.

the origin and intensity of the spectral features. The intensity of the peak resulting from transitions to 5s orbitals is higher in the theory than in the experimental result. This could be a result of differing broadening effects for the semi-core 5s orbitals and the valence-band 5d orbitals, which can influence experimental results. The same broadening was applied for both signals in the theoretical calculation.

Since the $Ce^{IV}$ system exhibits substantial charge-transfer character, leading to a ground state that cannot be adequately represented within the present TDDFT method, the corresponding VB-RIXS spectra was not included in the calculation. A quantitative description would require explicit inclusion of ligand-to-metal and metal-to-ligand charge-transfer configurations in the effective Hamiltonian analogous to approaches previously developed for mixed-valence and strongly covalent transition metal systems.[40] Such treatments are, in principle, feasible and have been successfully applied using empirical charge-transfer multiplet models for $Ce^{IV}$ systems.[34, 41] Extension of the LFDFT method[42] toward non-empirical account of the charge transfer electronic structure is currently under development by some of us, but requires additional paradigm and computational advances beyond the scope of the present work.

**X-ray induced changes to the electronic structure and bonding of Ce.** During measurement, noticeable changes in the spectra of the cerium complexes upon irradiation with X-ray photons occurred (Figure 8). Stabilizing the compounds sufficiently long for recording of HR-XANES and VB-RIXS spectra was possible by adjusting the intensity of the incident X-ray beam and cooling the samples to -95°C (cf. SI for details). However, spectral changes observed outside of the stable window of 20 ($[Ce^{III}\{PhC(N^tBu)_2\}_3]$) or 24 ($[Ce^{IV}\{PhC(N^tBu)_2\}_3][Al(OC_4F_9)_4]$) minutes, can give us insight into how the electronic structure of these compounds is changed by photochemical effects. Figure 8 depicts Ce $L_3$-edge HR-XANES spectra of the $Ce^{III}$ and $Ce^{IV}$ compounds measured using high-energy resolution and low photon flux

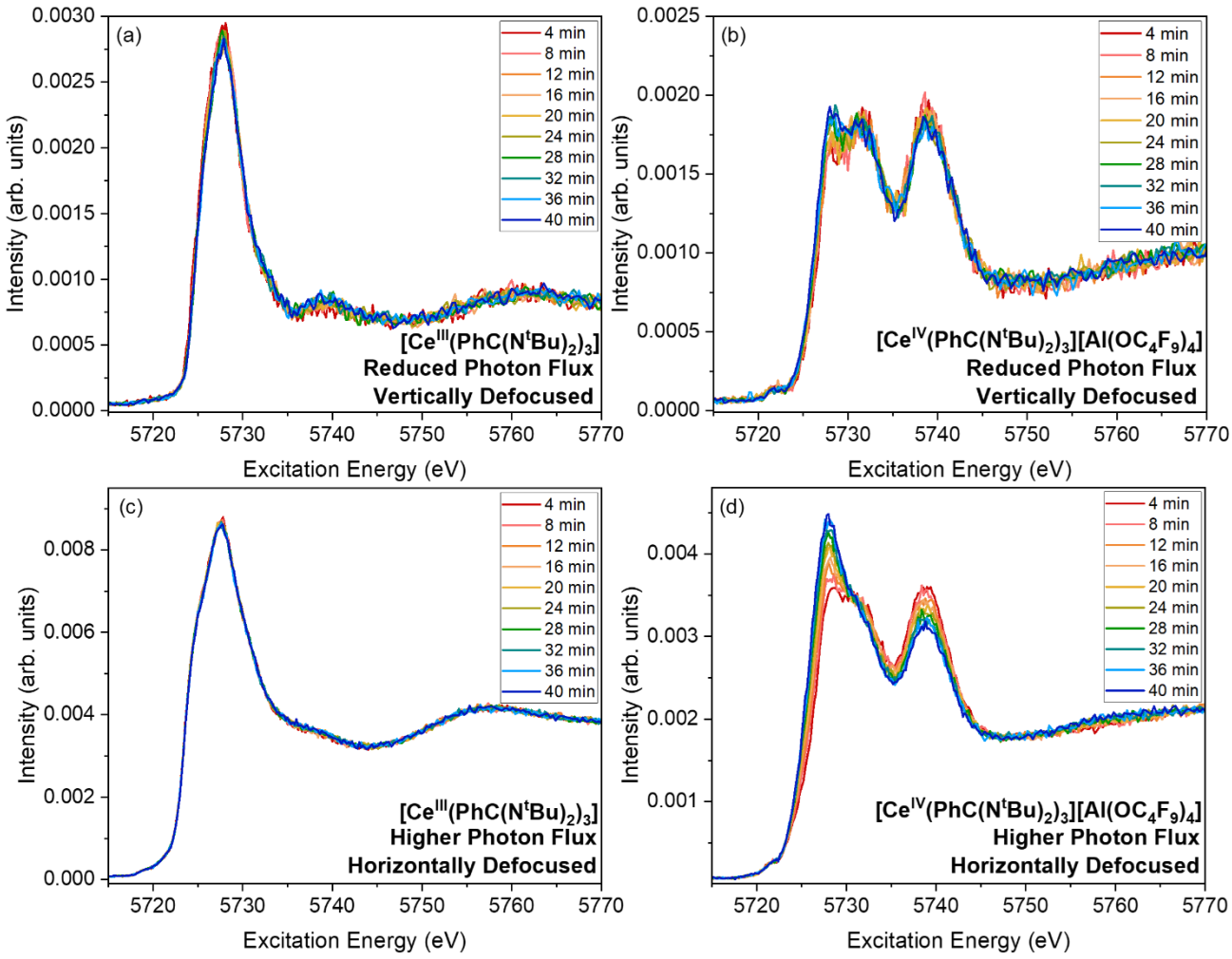


**Figure 8**. In every part of the figure (a-d) a set of ten Ce $L_3$-edge HR-XANES spectra, each measured for 4 minutes, are displayed. Spectra of (a) $[Ce^{III}\{PhC(N^tBu)_2\}_3]$ and (b) $[Ce^{IV}\{PhC(N^tBu)_2\}_3][Al(OC_4F_9)_4]$ are recorded with a photon absorber and a vertically defocused X-ray beam, which leads to reduced photon-induced spectral changes and increased experimental resolution (compared to horizontal defocusing. Spectra of (c) $[Ce^{III}\{PhC(N^tBu)_2\}_3]$ and (d) $[Ce^{IV}\{PhC(N^tBu)_2\}_3][Al(OC_4F_9)_4]$ recorded with no absorber and a horizontally defocused beam, which allow to clearly observe photon-induced spectral changes with reduced experimental resolution, respectively.

(a and b) and low-energy resolution and high photon flux (c and d). The Ce $L_3$-edge HR-XANES of $[Ce^{III}\{PhC(N^tBu)_2\}_3]$ reveals only a very slight increase in intensity of the spectral feature at about 5740 eV (Figure 8, (a)). It is in the same energetic position as the $4f^0$ signal (second white line) of the $[Ce^{IV}\{PhC(N^tBu)_2\}_3][Al(OC_4F_9)_4]$ spectrum (Figure 8, (b)). The spectrum of the $Ce^{III}$ complex does not show changes in the WL shape or intensity and the position of the first post-edge resonance does not change (Figure 8, (a) and (c)). While the changes to the first post-edge feature start earlier than changes in the spectrum of the $Ce^{IV}$, they are much less significant and progress more slowly. This indicates a change in electronic structure in which the make-up of the *5d*-dominated unoccupied molecular orbitals varies, but without a change in atomic geometry or bond length involving the Ce atom. Interestingly, the higher photon flux, but lower experimental resolution and the same irradiation time did not lead to any significant changes in the $Ce^{III}$ spectrum (Figure 8, (c)). This demonstrates that the high-energy resolution is necessary for detection of small spectral changes.

For the $Ce^{IV}$ complex, multiple staggered changes are visible (Figure 8, (b) and (d)). The changes begin with a rise in intensity of the lower energy feature in the $4f^1\underline{L}$ WL at ca 5728 eV. Until the intensity of the lower energy feature reaches that of the higher energy split, the $4f^0$ WL does not show significant changes. Once the intensity of the lower energy split exceeds that of the higher energy split, the intensity of the $4f^0$ WL at about 5739 eV begins to sink (Figure 8, (b)). These changes occur with initially unchanged post-edge features, indicating a changed electronic structure with an intact $Ce^{IV}$ local atomic structure and $Ce^{IV}$-ligand bond length. In a third step, visible later, the post-edge position begins to move to lower energies, indicating a collapse of the physical structure and the lengthening of first coordination shell bonds, towards the post-edge position (and bond length) of the $Ce^{III}$ complex (Figure 8, (d)). The change in the position of the first post-edge resonance, and thus the disintegration of the structural integrity of the complex, specifically the local environment of the Ce central atom, being a separate process from the changes in the WL regions is particularly interesting, indicating a level of coordination stability beyond changes in electronic structure. It appears that damage to the outer regions of the complex takes place before the structure and geometry of the local environment of the Ce atom change.

The VB-RIXS signal patterns of both complexes also change with increased irradiation time and intensity (cf. Figure S24), though this seems to be delayed or less sensitive, as small changes in the splitting of the $4f^1\underline{L}$ WL in the HR-XANES of $[Ce^{IV}\{PhC(N^tBu)_2\}_3][Al(OC_4F_9)_4]$ do not result in differences in the VB-RIXS when excited at the energy of the $4f^1\underline{L}$ WL (Figure S24, (b)). Once the changes become more prominent, feature B.I decreases in intensity, while features B.II and B.III increase in intensity (Figure S24 (d)). Interestingly, $[Ce^{III}\{PhC(N^tBu)_2\}_3]$ shows only barely visible changes upon a much longer irradiation time with the same intensity of irradiation (Figure S24 (c)). Signals A.I and A.II, which are energetically in the same position as B.II and B.III, decrease in intensity. Additionally, the separation between the elastic peak and A.I decreases due a shoulder appearing at the lower energies of the elastic peak, indicating an increase in intensity at the energy where B.I is for the $Ce^{IV}$

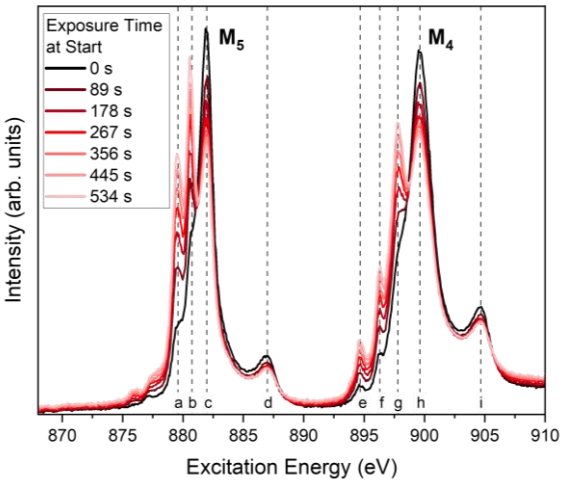


**Figure 9.** Changes in the Ce $M_{4,5}$-spectrum of $[Ce^{IV}\{PhC(N^tBu)_2\}_3][Al(OC_4F_9)_4]$, measured via total electron yield, after increasing amounts of irradiation. Prominent spectral features are labelled with lowercase letters a through i.

complex (Figure S24 (c)). This suggests that the electronic structure underlaying the *5d* electron density participating in bonding shifts toward that of the opposite formal oxidation state, particularly once HR-XANES show significant changes. However, it is obvious that this effect is significantly stronger and occurs more rapidly for the $Ce^{IV}$ amidinate than the $Ce^{III}$ amidinate.

These findings are complemented by soft X-ray measurements at the Ce $M_{4,5}$-edge of $[Ce^{IV}\{PhC(N^tBu)_2\}_3][Al(OC_4F_9)_4]$ (Figure 9), where significant changes are visible upon irradiation. Measurements at the $M_{4,5}$-edge are useful in probing the Ce *4f* states of compounds. These states are very local, and the spectra are dominated by *4f* multiplet structures,[18, 42-44] which makes the method very sensitive to the *4f* occupation. The measured spectrum of $[Ce^{IV}\{PhC(N^tBu)_2\}_3][Al(OC_4F_9)_4]$ is very similar to the reported spectrum of $CeO_2$,[45] indicating very similar configurations for these two compounds, also corroborating the findings of the hard X-ray measurements. Therefore, these spectra also show sensitivity to electron donation from the ligand to the metal through covalent bonding interaction and a mixed $3d^94f^2\underline{L}$ and $3d^94f^1$ final state configuration is necessary to also reproduce features d and i of the spectra.[46] When observing how the spectrum changes, a gradual change towards features present in the spectrum of the $Ce^{III}$ amidinate is visible (cf. Figure S28). This matches results at the $L_3$-edge and is especially obvious in the intensity increase in features a, b, e, f and g. Spectral changes at these edges indicate changes in electronic structure involve both *5d* and *4f* electron density. The time scale at which changes take place is much smaller at these energies than at the Ce $L_3$-edge, which is a result of a higher radiation dose rate, due to a higher flux, a higher cross section, and lower attenuation length for the soft X-ray measurements taken at X-SPEC.

In summary, these observations suggest an electronic structure that is modulated under photon influence long before significant geometric structural changes close the Ce central atom occur, in each case growing closer to the electronic structure of the respective sister complex. Notably,

the $Ce^{IV}$ compound shows pronounced sensitivity to this type of change.

**Ce local coordination environment.** Finite difference method near edge structure (FDMNES) calculations based on experimental structures determined using X-ray diffraction (XRD) were used to model the transitions in the HR-XANES spectra of the complexes (Figure 10). For $[Ce^{III}\{PhC(N^tBu)_2\}_3]$, the calculation is able to model the features of the spectrum well, with the underlying splitting of the WL clearly visible, and both the first feature after the WL and the first post-edge resonance in the correct position (Figure 10, (a)). For the $Ce^{IV}$ complex, the calculation, when shifted to the first WL (Figure 10, (b)), is able to model the splitting of the first WL ($4f^1\underline{L}$) feature well, though the intensity ratio differs. The position of the first post-edge resonance is not modelled correctly and the second ($4f^0$) WL feature is completely absent. These discrepancies were expected and are due to the limitations of the multiple-scattering theory of modelling the multiconfigurational electronic structure involved in $Ce^{IV}$-spectroscopy. When shifting the calculations to higher energies for alignment with the $4f^0$ WL (Figure 10, (c)), the position of the first post-edge resonance aligns with the calculated spectrum, though this is more visible when comparing longer-range conventional spectra (cf. SI, Figure S29). The good agreement of the post-edge features for both $Ce^{III}$ and $Ce^{IV}$ ($4f^0$), including longer energy range conventional spectra, provides additional confirmation that the compounds studied with HR-XANES have not undergone any decomposition during the sample transfer. Results of calculations that take quadrupole transitions into account compared to results of dipole-only calculations show that quadrupole transitions mainly play a part in the pre-edge region, though this region is still largely dominated by dipole transitions (cf. SI, Figure S30). This is likely a result of $4f/5d$ mixing and dipole transitions into resulting molecular orbitals. This energy region of the density of states calculated in the FDMNES process is dominated by f and d contributions, which supports this assumption (cf. SI, Figure S31).

**Quantum chemical studies of bonding interactions.** Geometry optimizations were performed for the amidinate ligand and the two complexes $[Ce^{III}\{PhC(N^tBu)_2\}_3]$ and $[Ce^{IV}\{PhC(N^tBu)_2\}_3]^+$. Note that in the optimized structures (Table S9 and Table S10), single symmetry-equivalent Ce–N bond length, single N–C bond length within the amidinate ligand (where the central carbon atom bridges the two nitrogen donors), and one N–C–N bond angle are obtained as results of the symmetry restrictions ($D_3$ point group). In contrast, the experimental XRD structures display slight distortions from the ideal symmetry, leading to six individual Ce–N distances, six N–C bond lengths, and three independent N–C–N angles. For $[Ce^{III}\{PhC(N^tBu)_2\}_3]$, the calculated Ce–N bond length of 2.502 Å agrees well with the experimental values ranging from 2.488 to 2.536 Å (average 2.513 Å). Likewise, the computed N–C bond length of 1.329 Å closely matches the experimental range of 1.328–1.336 Å (average 1.332 Å), while the calculated N–C–N angle of 114.55° is consistent with the experimental values of 113.4–114.3° (average 113.89°). A similarly good agreement is obtained for $[Ce^{IV}\{PhC(N^tBu)_2\}_3]^+$. The calculated Ce–N bond length of 2.374 Å reproduces well the experimental distances ranging from 2.363 to 2.403 Å (average 2.392 Å). The calculated N–C bond length (1.331 Å) and N–C–N bond angle (113.13°) are also consistent with the experimental averages of 1.341 Å and 113.0°, respectively. Importantly, both experiment and theory show a clear contraction of the Ce–N bond upon oxidation from $Ce^{III}$ to $Ce^{IV}$, reflecting the increased effective nuclear charge on the Ce center, and also smaller ionic radius of tetravalent Ce (0.87 Å ($Ce^{IV}$) versus 1.01 Å ($Ce^{III}$) in sixfold coordinated systems[32]), which strengthen the interaction with the amidinate nitrogen donors.

The frontier molecular orbitals of the amidinate ligand, which are primarily responsible for the metal-ligand interactions, are shown in the SI (Figure S32). The highest occupied molecular orbitals (HOMOs) consist of three distinct types: the HOMO corresponds to the delocalized π framework of the N-C-N unit and is largely composed of nitrogen *2p* orbitals, which will be oriented perpendicular to the metal–nitrogen bond axis, giving rise to an anisotropic π-donor character. In contrast, the HOMO-1 and HOMO-2 orbitals are predominantly nitrogen-centered lone pairs and thus constitute the σ -donor framework. These two sets of lone-pair orbitals differ in their internal phase relationship within the ligand, corresponding to the in-phase symmetric and the out-of-phase antisymmetric combinations of the nitrogen lone pairs.

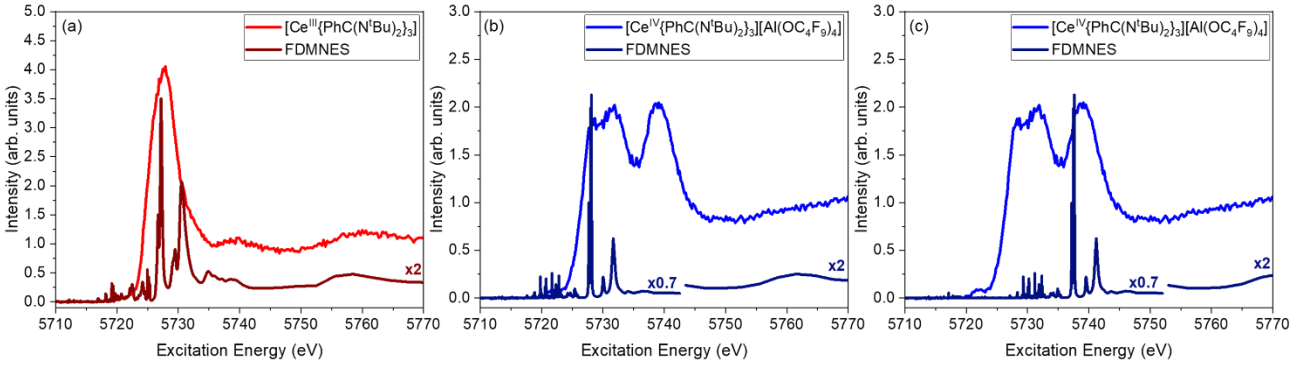


**Figure 10.** Experimental Ce $L_3$-edge HR-XANES spectra compared FDMNES calculations. The calculations are based on the determined XRD structure of (a) $[Ce^{III}\{PhC(N^tBu)_2\}_3]$ and (b) and (c) $[Ce^{IV}\{PhC(N^tBu)_2\}_3][Al(OC_4F_9)_4]$. In (a) and (b), the calculation results are shifted to match the most intense absorption peak (WL), in (c) the calculated spectrum is shifted by 9.5 eV in comparison to (b) to match the second WL feature. The calculations are scaled (2x in (a); 0.7x in the pre-edge and WL region and 2x in the post-edge region in (b) and (c)) to make the comparison more visible.

When coordinated with the Ce center, the amidinate frontier orbital sets generate symmetry-adapted linear combinations (SALC) that transform to $a_1$ and e irreducible representations of the $D_3$ point group (Figure S33 and S34). These ligand-based SALCs form the basis for interaction with the cerium valence orbitals, where the σ-donor lone pairs primarily overlap with Ce *5d* orbitals to establish the bonding framework, while the higher-lying π orbitals interact more weakly and anisotropically, contributing to the high-lying HOMOs of the complexes, and also enabling limited ligand-to-metal pi donation in $[Ce^{IV}\{PhC(N^tBu)_2\}_3]^+$.

Figure 11 presents the calculated MO energy diagrams of $[Ce^{III}\{PhC(N^tBu)_2\}_3]$ and $[Ce^{IV}\{PhC(N^tBu)_2\}_3]^+$ in $D_3$ symmetry, with energies relative to the HOMO that is set to 0 eV in both systems. The $[Ce^{III}\{PhC(N^tBu)_2\}_3]$ calculation was performed in a spin-unrestricted formalism, resulting in two series of orbitals corresponding to alpha and beta spins. The singly occupied MO (SOMO) of $[Ce^{III}\{PhC(N^tBu)_2\}_3]$ is primarily characterized by Ce *4f* orbitals (*4fy*$(3x^2\text{-}y^2)$) (cf. SI, Figure S34). The higher-energy occupied orbitals in both $[Ce^{III}\{PhC(N^tBu)_2\}_3]$ and $[Ce^{IV}\{PhC(N^tBu)_2\}_3]^+$ are predominantly ligand-centered and consist largely of nitrogen *2p* orbitals. These orbitals correspond to the π-orbital framework SALC of the N-C-N backbones of the amidinate ligands. In $[Ce^{III}\{PhC(N^tBu)_2\}_3]$, the empty *4f* orbitals are distributed close to the energy range of the *5d* orbitals, whereas in $[Ce^{IV}\{PhC(N^tBu)_2\}_3]^+$, the empty *4f* orbitals are stabilized at lower energy value, reflecting the increased effective nuclear charge in the tetravalent state.

In $[Ce^{III}\{PhC(N^tBu)_2\}_3]$ and $[Ce^{IV}\{PhC(N^tBu)_2\}_3]^+$, the metal-ligand bonding is dominated by σ-donation from the amidinate N atoms, with negligible π contribution. In $[Ce^{IV}\{PhC(N^tBu)_2\}_3]^+$ we observe slight mixing between the ligand π SALCs and the $4fz^2x$ and $4fz^2y$ orbitals, whose lobes are oriented to interact with the nitrogen π framework. This weak interaction gives rise to small metal character to the HOMO (< 5%), leading to stronger Ce-N bond covalency without significantly perturbing the delocalized π network of the ligand. Simultaneously, the σ-framework remains strongly stabilized in both formal oxidation states due to effective overlap with Ce *5d* (and *6s*/*6p*) orbitals.

We observe that the redistribution of electron density in $[Ce^{IV}\{PhC(N^tBu)_2\}_3]^+$ where part of the ligand π density is delocalized onto the metal lowers the energy of the HOMO relative to the isolated ligand orbitals. This stabilization explains the observed shorter Ce-N bond distances and greater covalent character in the tetravalent complex. In contrast, in $[Ce^{III}\{PhC(N^tBu)_2\}_3]$, with its localized π HOMO and largely ionic *4f*-centered SOMO, remains primarily stabilized by σ-donation, resulting in longer bond length and weaker covalency. Overall, the MO diagrams reveal that formal oxidation state modulates both the participation of metal orbitals in bonding and the delocalization of the electron density from the ligand π network.

**Bonding Analysis.** To understand the mechanism of the metal-ligand interaction in the complexes, we have performed two different bond analyses. This includes natural bond order/natural localized molecular orbital (NBO/NLMO) methods[47] and quantum theory of atoms in molecules (QTAIM).[48] The calculations were carried out with DFT and hybrid PBE0 functional. Figures 12 and 13 display the NLMOs for $[Ce^{III}\{PhC(N^tBu)_2\}_3]$ and

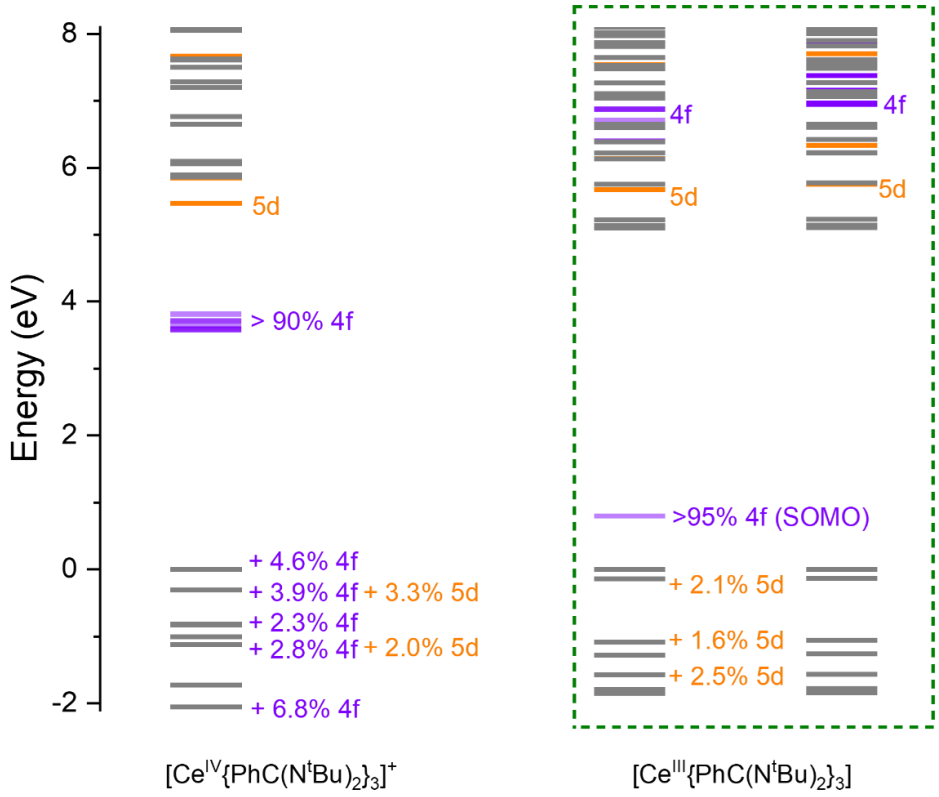


**Figure 11**. Energetic positions of molecular orbitals in $[Ce^{III}\{PhC(N^tBu)_2\}_3]$ and $[Ce^{IV}\{PhC(N^tBu)_2\}_3]^+$ relative to their highest occupied molecular orbitals (HOMO); color indicates the predominant atomic orbital involved in the molecular orbitals. The relative Ce *4f* and *5d* contributions are marked and the singly occupied molecular orbital (SOMO) in the $Ce^{III}$ complex is noted.

$[Ce^{IV}\{PhC(N^tBu)_2\}_3]^+$, respectively, illustrating the primary sigma and pi bonding interactions between Ce and the amidinate ligands. The figure also shows the percent character for Ce atomic orbitals, which reveal a significant shift in orbital composition. That is the contribution from Ce doubles from $[Ce^{III}\{PhC(N^tBu)_2\}_3]$ to $[Ce^{IV}\{PhC(N^tBu)_2\}_3]^+$, which suggests a more covalent interaction in the latter. Table 1 summarizes the topological properties of the electron density at the bond critical point for the Ce-N interaction. Transitioning from $[Ce^{III}\{PhC(N^tBu)_2\}_3]$ to $[Ce^{IV}\{PhC(N^tBu)_2\}_3]^+$, the electron density (ρ(r)) increases by 37%, accompanied by a 53% raise in the delocalization index ((δ), signaling a strengthening of the Ce-N bond. The total electronic energy density (H(r)) becomes significantly more negative (-140%), while shifting the |V|/G ratio downward by 17%. Furthermore, the bond ellipticity (ε) increases by 160%, reflecting a substantial gain in pi-character and anisotropy in $[Ce^{IV}\{PhC(N^tBu)_2\}_3]^+$.

Oxidation from $Ce^{III}$ to $Ce^{IV}$ induces significant changes in the electronic structure and bonding metrics of the Ce–N interactions. As stated earlier, the Ce–N bond distances contract from 2.502 Å in $[Ce^{III}\{PhC(N^tBu)_2\}_3]$ to 2.374 Å in $[Ce^{IV}\{PhC(N^tBu)_2\}_3]^+$, representing a 5.1% decrease in bond length, consistent with the smaller ionic radius and greater effective nuclear charge of $Ce^{IV}$. This contraction facilitates improved metal–ligand orbital overlap and is reflected in the NLMO analysis, which shows that cerium participation in the nitrogen donor orbitals increases from approximately 2–4% in $[Ce^{III}\{PhC(N^tBu)_2\}_3]$ to 7.5–8.0% in $[Ce^{IV}\{PhC(N^tBu)_2\}_3]^+$. In both oxidation states, the metal contributions derive from hybridized orbitals with dominant *4f/5d* character, although the greater overall metal contribution in $[Ce^{IV}\{PhC(N^tBu)_2\}_3]^+$ indicates enhanced orbital mixing upon oxidation.

Inspection of the NLMO compositions provides further insight into the origin of the enhanced covalency in $[Ce^{IV}\{PhC(N^tBu)_2\}_3]^+$. In both complexes, the Ce acceptor hybrids involved in Ce–N bonding contain substantial admixture of both 4*f* and 5*d* character; however, the $Ce^{IV}$ analog exhibits not only greater overall metal participation within the donor NLMOs, but also a higher fractional contribution from 4*f* orbitals within the metal hybrid acceptor set. Specifically, whereas the Ce-centered donor acceptor hybrids in $[Ce^{III}\{PhC(N^tBu)_2\}_3]$ contain approximately 40–60% 4*f* character, the analogous hybrids in $[Ce^{IV}\{PhC(N^tBu)_2\}_3]^+$ exhibit 58–63% 4*f* composition. This finding indicates that the enhanced orbital mixing in $[Ce^{IV}\{PhC(N^tBu)_2\}_3]^+$ is not solely attributable to greater participation of diffuse 5*d* orbitals, but also reflects measurable engagement of the formally vacant $Ce^{IV}$ 4*f* manifold in bonding.

The increased 4*f* contribution upon oxidation is notable given the traditional view of lanthanide 4*f* orbitals as largely core-like and nonbonding. However, cerium represents a unique case among the lanthanides due to the comparatively diffuse nature of its early-series 4*f* orbitals and the accessibility of a formal $4f^0$ oxidation state in $Ce^{IV}$. Oxidation from $Ce^{III}$ to $Ce^{IV}$ lowers the energy of the metal-centered acceptor orbitals while simultaneously contracting the Ce–N bond distances from 2.502 to 2.374 Å, thereby improving both energetic and spatial overlap between the nitrogen donor lone pairs and the Ce acceptor manifold. As a result, the vacant 4*f* orbitals become sufficiently accessible to

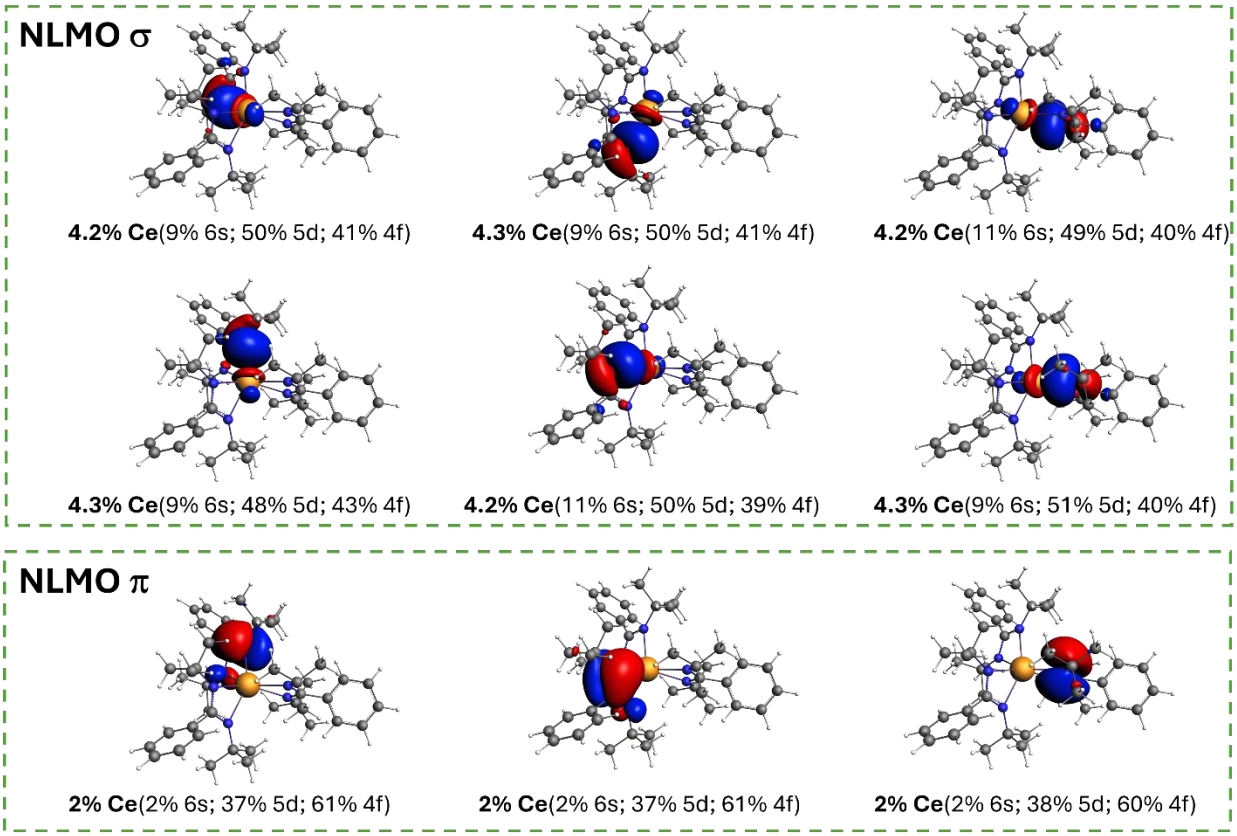


**Figure 12.** Selected NLMOs showing the main interactions responsible for the Ce-N bonding in $[Ce^{III}\{PhC(N^tBu)_2\}_3]$.

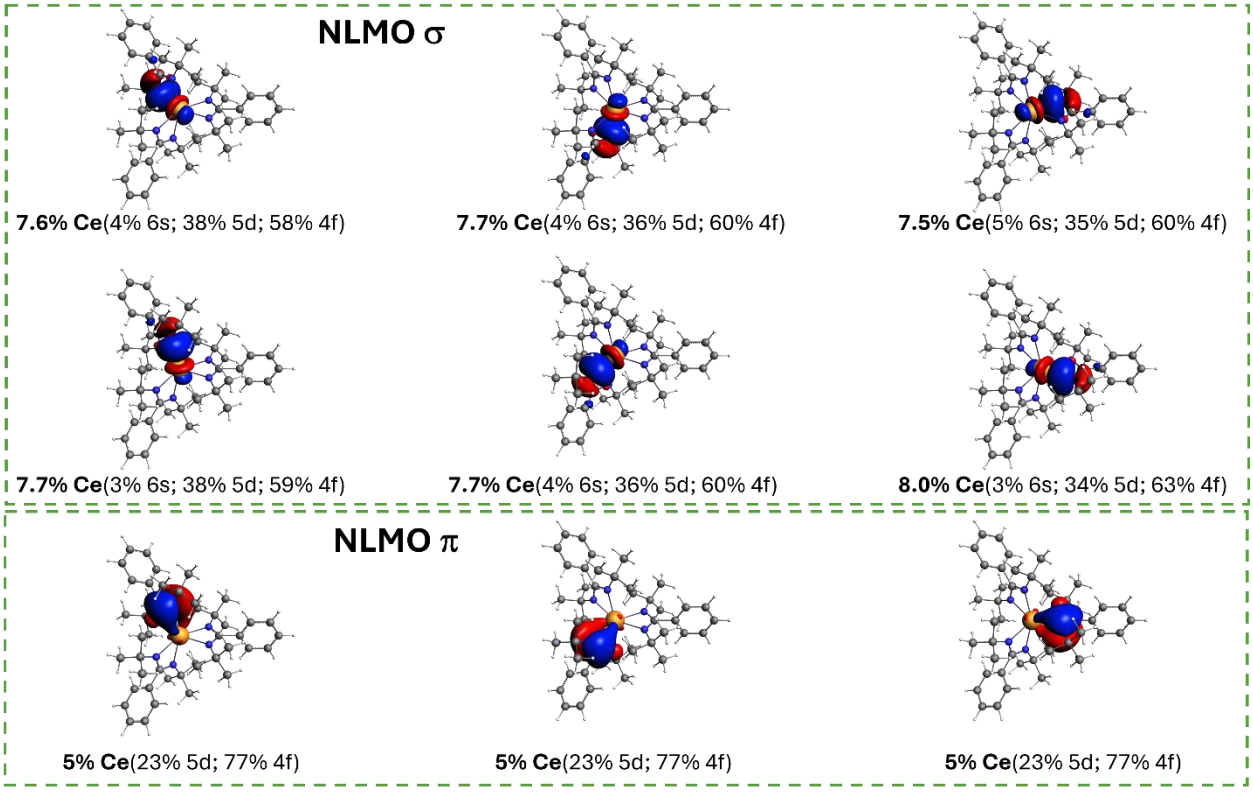


**Figure 13.** Selected NLMOs showing the main interactions responsible for the Ce-N bonding in $[Ce^{IV}\{PhC(N^tBu)_2\}_3]^+$.

**Table 1.** Selected QTAIM metrics for $[Ce^{III}\{PhC(N^tBu)_2\}_3]$ and $[Ce^{IV}\{PhC(N^tBu)_2\}_3]^+$: electron density (ρ(r) in eÅ$^{-3}$), potential energy density kinetic energy density, total energy densities (V(r), G(r), H(r) in kcal mol$^{-1}$Å$^{-3}$), ratio V/G, ellipticity (ε), and delocalization index (δ(r)).

| Bond | ρ(r) | V(r) | G(r) | H(r) | V/G | H/ρ(r) | Ellipticity | δ(r) |
|---|---|---|---|---|---|---|---|---|
| $Ce^{III}$-N | 0.3742 | -1038.7 | 858.5 | -180.2 | -1.2 | -481.5 | 0.086 | 0.344 |
| $Ce^{IV}$-N | 0.5130 | -1628.6 | 1195.8 | -432.8 | -1.4 | -843.7 | 0.224 | 0.528 |

participate in donor–acceptor interactions, contributing to the enhanced covalent character observed in $[Ce^{IV}\{PhC(N^tBu)_2\}_3]^+$.

Consistent with the NLMO results, QTAIM analysis reveals substantial strengthening of the Ce–N bonding interaction in $[Ce^{IV}\{PhC(N^tBu)_2\}_3]^+$ relative to $[Ce^{III}\{PhC(N^tBu)_2\}_3]$. The electron density at the bond critical point increases by 37%, while the potential energy density becomes significantly more negative, indicating stronger attractive interactions. Most notably, the total energy density H(r) becomes 140% more negative, supporting greater bond stabilization and enhanced covalent character in the $Ce^{IV}$ complex. The |V(r)|/G(r) ratio increases from 1.2 to 1.4, while the delocalization index increases by 53%, further indicating greater electron sharing between cerium and the nitrogen donors in $[Ce^{IV}\{PhC(N^tBu)_2\}_3]^+$. Collectively, these data demonstrate that oxidation to $Ce^{IV}$ strengthens the Ce–N interaction not only through increased electrostatic attraction but also through greater orbital-mediated covalency.

## CONCLUSION

In this work, we successfully synthesized and characterized a pair of homoleptic complexes of $Ce^{III}$ and $Ce^{IV}$ ions. Advanced X-ray spectroscopic techniques provided insights into their electronic structures and bonding interaction, while theoretical modeling allowed us to quantitatively assess bonding properties and accurately characterize the X-ray spectral features. This work establishes a direct spectroscopic correlation between formal oxidation state and metal-ligand bond covalency and demonstrates that formal oxidation state decisively modulates bonding in isostructural cerium tris(amidinate) complexes, with the $Ce^{IV}$ compound exhibiting enhanced *4f* and *5d* participation in bonding covalent interactions relative to its $Ce^{III}$ analogue.

Ce $L_3$-edge HR-XANES provide insight into the unoccupied *4f*- and *5d*-derived states and their energetic differences, as well as intermediate-state effects such as the multiconfigurational character of the $Ce^{IV}$ intermediate state. Indirect information about Ce *4f* and *5d* participation in bonding can be derived from these spectra. Analysis of the energy shift between the pre-edge (4f-derived) and main edge (*5d*-derived) transitions, ΔE(*5d*, *4f*), of Ce $L_3$-edge HR-XANES spectra indicates increasing bond covalency in the order $CeCl_3$ < $[Ce^{III}\{PhC(N^tBu)_2\}_3]$ < $[Ce^{IV}\{PhC(N^tBu)_2\}_3][Al(OC_4F_9)_4]$ ≈ $CeO_2$. These findings are further validated by theoretical modeling by carrying out bond analysis and natural localized molecular orbitals computation. Results show that both $Ce^{III}$ and $Ce^{IV}$ complexes have measurable interaction with the ligand via the *5d* orbitals. This results from an orbital-overlap driven bond covalency mechanism. The extent of mixing between Ce *5d*

and N *2p* orbitals increases from $Ce^{III}$ to $Ce^{IV}$ complexes, which is primarily due to the shortening of the Ce-N bond length in the series. Furthermore, we establish that the Ce *4f* orbitals play important role in the $Ce^{IV}$ complex, modulating its electronic structures to exhibit a strong ligand-to-metal charge transfer effect. This results from an energy-degeneracy driven bond covalency mechanism where the Ce *4f* and N *2p* orbitals are found at very close energy levels. In that, the HR-XANES spectra show double WL features that are very characteristic of $CeO_2$ and other reported $Ce^{IV}$ complexes. Going a step further, we have collected VB-RIXS spectra of the two complexes, and show for the first time for Ce that it is possible to probe the occupied *5d*-derived states and quantitatively compare participation of Ce *5d* electron density in bonding for excitation at different energies. Comparison of spectra most closely reflecting the ground-state electronic structure shows that $[Ce^{IV}\{PhC(N^tBu)_2\}_3][Al(OC_4F_9)_4]$ exhibits greater *5d*-electron participation in bonding than $[Ce^{III}\{PhC(N^tBu)_2\}_3]$, reinforcing the conclusion that the $Ce^{III}$ complex has weaker covalent bonding contributions than the $Ce^{IV}$ complex.

Electronic and geometric structure changes were observed upon irradiation with X-rays for both $Ce^{III}$ and $Ce^{IV}$ complexes. It was demonstrated that the intensity distribution of the $Ce^{IV}$ $4f^1\underline{L}$ double-peak white-line structure of the Ce $L_3$-edge HR-XANES spectrum changes first, followed by changes in the VB-RIXS spectra and the local geometric structure around the Ce atoms. The final step is reduction to $Ce^{III}$. Moreover, it was found that the $Ce^{IV}$ complex is influenced and reduced to a significantly greater extent than the $Ce^{III}$ compound is oxidized. These results clearly suggest that photon-induced charge transfer occurs within the complexes while the compounds remain structurally intact within the local Ce atomic environment, at least during the initial phase of the irradiation process.

We presented the first combined Ce $L_3$-edge HR-XANES and quantitative VB-RIXS study, complemented by Ce $M_{4,5}$-edge XANES, directly comparing bonding properties and covalency for isostructural $Ce^{III}$ and $Ce^{IV}$ metal–N-donor ligands compounds. These findings provide detailed insight into oxidation-state-dependent bonding in molecular lanthanide systems and inform strategies for tuning electronic structure and physicochemical properties through redox control.

## EXPERIMENTAL SECTION

**Synthesis of the $Ce^{III}$ compound.** For the synthesis of $[Ce^{III}\{PhC(N^tBu)_2\}_3]$, $[Ce(BH_4)_3(thf)_3]$ (841 mg, 2.10 mmol, 1.0 equiv) was combined with $Li(^tBuN)_2CPh$ (1.50 g, 6.29 mmol, 3.0 equiv) in THF (30 mL) and the reaction mixture heated to 80 °C for 24 h. Over the course of the reaction, the colorless solution gradually turned bright yellow, accompanied by the formation of a $LiBH_4$ precipitate. Following removal of the solvent under reduced pressure, the residue was taken up in *n*-heptane (40 mL) and filtered hot through a P4 silica frit. The clear filtrate was concentrated to approximately 20 mL and reheated until homogeneity was achieved. Slow cooling of the solution to −30 °C overnight yielded $[Ce^{III}\{PhC(N^tBu)_2\}_3]$ as yellow crystalline material (1.41 g, 80%). **$^1$H NMR** (400 MHz, THF-$d_8$) δ = 13.84 (s, 6H, Ar-H), 9.78 (s, 6H, Ar-H), 9.14 (s, 3H, Ar-H), - 3.00 (s, 54H, $^t$Bu-H). **$^{13}$C NMR** (75 MHz, THF-$d_8$) δ = 137.77 (Ph), 131.54 (Ph), 131.05 (Ph), 31.30 ($^t$Bu).

**Synthesis of the $Ce^{IV}$ compound.** In order to synthesize $[Ce^{IV}\{PhC(N^tBu)_2\}_3][Al(OC_4F_9)_4]$, a cooled mixture of $[Ce^{III}\{PhC(N^tBu)_2\}_3]$ (100 mg, 0.120 mmol, 1.0 equiv) and $[Ag(dcm)][Al(OC_4F_9)_4]$ (139 mg, 0.120 mmol, 1.0 equiv) was brought to −89 °C. Addition of *o*-difluorobenzene (10 mL) to the solids immediately induced a color change from yellow to dark green-blue. The suspension was then allowed to warm to room temperature and stirred for 72 h. Afterwards, the reaction mixture was filtered through a P4 silica frit, and the filtrate concentrated to ca. 3 mL. The concentrated solution was carefully layered with *n*-heptane (10 mL) and left undisturbed for several days, resulting in the crystallization of $[Ce^{IV}\{PhC(N^tBu)_2\}_3][Al(OC_4F_9)_4]$ as dark-blue material which was afterwards washed with *n*-heptane (147 mg, 68%). **$^1$H NMR** (400 MHz, THF-$d_8$) δ = 7.60 – 7.43 (m, 15H, Ar-H), 1.35 (s, 54H, $^t$Bu-H). **$^{13}$C NMR** (75 MHz, THF-$d_8$) δ = 130.28 (Ph), 34.97 ($^t$Bu).

**HR-XANES and VB-RIXS Experiments.** HR-XANES and VB-RIXS of cerium at the $L_3$-edge were measured at the SUL-X beamline of the KIT Light Source Karlsruhe, Germany. The beamline's radiation source is a 27-pole wiggler and the incoming beam is then monochromatized by a fixed-exit Si(111) double-crystal monochromator. Using slits and horizontally and vertically focusing bending mirrors (a Kirkpatrick-Baez focusing system), the incoming beam size was adjusted to ca 0.2 mm horizontally by 1.2 mm vertically. Measurements were performed using a single analyzer crystal X-ray emission spectrometer in focusing horizontal Rowland circle geometry involving detection of a photoemission energy chosen using a striped spherically bent Si(211) crystal analyzer with a 0.5 m bending radius at the 422 reflection. A two-point calibration was performed using the Cr $KM_{2,3}$ emission line of a Cr metal foil (PyMCA 5946.7 eV[49]) and the Mn $KM_{2,3}$ line of a Mn metal foil (PyMCA 6490.4 eV[49]) Detection took place using an avalanche photodiode (FMB Oxford, APD Detector HD 5X5C) with a 70 µm Kapton window at the maximum of $CeL_3N_{4,5}$ emission line (PyMCA 5613.4 eV[49], Bragg angle of 85.01°). The sample, crystal and detector were positioned so that the angle between the incoming beam and the crystal surface is 180° and the Rowland circle is tilted 8° against the beam plane in order to allow it to pass beneath the crystal, through the holder, to reach the sample, which results in an overall 172° σ ("backscattering") geometry, σ referring to a geometry in which the polarization vector of the incoming photons is (close to) linear and lies in the synchrotron plane while being perpendicular to the surface normal of the scattering plane.[50] Measurement took place under high vacuum ($10^{-5}$ mbar) to minimize absorption of X-ray radiation by air molecules. The measurement of an elastic line of an Au foil at 5614.3 eV (value after calibration) showed a spectrometer resolution of 0.9 eV. For measurements of $[Ce^{IV}\{PhC(N^tBu)_2\}_3][Al(OC_4F_9)_4]$and $[Ce^{III}\{PhC(N^tBu)_2\}_3]$ a 0.5 mm graphite absorber was used to reduce beam intensity instead of the standard 0.1 mm graphite absorber used for reference samples. Parallel to high resolution measurements, conventional measurements were taken using a 7-element silicon drift detector (type Sirius, RaySpec) with the ROI set to measure the $L_3M_5$ emission line (PyMCA 4840.1 eV[49]). Samples were cooled to ca -95°C using a liquid-nitrogen based cryo set-up. Modified cryostat cells from CAT-ACT were used for measurement.[51]

Samples were drop-casted onto the anodized Al surface using dry toluene for $[Ce^{III}\{PhC(N^tBu)_2\}_3]$ and dry tetrahydrofurane for $[Ce^{IV}\{PhC(N^tBu)_2\}_3][Al(OC_4F_9)_4]$ and $SmI_2$, which was added to the cell as an indicator due to its stark color change from black to white upon contact with air. Transportation and preparation of samples took place under Ar atmosphere. Radiation damage tests were performed by collecting a series of HR-XANES spectra (eight 30 second scans, followed by ten four-minute scans and monitoring the spectral profile for changes with increasing time exposed to radiation. Subsequent measurements were then performed on fresh sample spots and limited to stable time frames to ensure data quality. Calibration of the excitation energy was performed using the first maximum of the first derivative of repeated XANES transmission measurements of a Vanadium foil at the K-edge (calibration to PyMCA literature value at 5465.1 eV[49]). The emission energy was calibrated using the reference (metallic Ce containing Flintstone) Ce $L_3N_{45}$ emission line (PyMCA 5613.4 eV[49]). VB-RIXS were calibrated by shifting the maximum of the elastic peak to the energy at which excitation took place.

HR-XANES data was processed by merging and normalizing using ATHENA from the DEMETER program package and exporting the normalized, not flattened spectrum.[52] Further data analysis was performed in OriginLab's OriginPro 2025.[53] VB-RIXS data was prepared for fitting in OriginPro 2025, where background subtraction was performed (cf. SI, Figure S25).

Soft X-ray XANES experiments at the Ce $M_{4,5}$ edge were performed at the X-SPEC beamline[54] at the KIT Light Source. Spectra were recorded in the total electron yield mode using the drain current of the samples and normalized to the incoming photon flux measured with a gold mesh upstream of the experimental chamber. For fast measurements, continuous energy scans (as opposed to step scans) were performed, which requires a simultaneous movement of soft X-ray monochromator and the undulator light source of the beamline.[55]

**Theoretical Calculations, Computational Details.** Calculations were performed with density functional theory (DFT) by using the Amsterdam Density Functional (ADF) code in the Amsterdam Modelling Suite (AMS).[38] The generalized gradient approximation (GGA) as a Perdew-Burke-Ernzerhof (PBE) formulation[56] and the hybrid PBE0 functional[57] were used. All-electron Slater-type orbital (STO) basis sets of triple-zeta quality widened with two polarization functions plus an extra f-STO (TZ2P+) for Ce and with a single polarization function (TZP) for C, N and H were used to expand molecular orbitals.[38] The Zeroth-Order Regular Approximation (ZORA) of the Dirac equation was used to implement relativistic corrections in both the scalar and spin-orbit levels of theory.[58] Dispersion forces were taken into account via the Grimme correction in its Becke-Johnson parametrization and its D3 formulation.[59]

**Geometry Optimization.** Molecular geometries of $[Ce^{III}\{PhC(N^tBu)_2\}_3]$ and $[Ce^{IV}\{PhC(N^tBu)_2\}_3]^+$ were optimized using GGA PBE[56] and PBE0[57] DFT functionals and scalar relativistic level. The complexes have identical structures, with 121 atoms, optimized geometries are available in the SI, Table S8, Table S9 and Table S10. The calculations were carried out by using Density-Functional Theory (DFT) as implemented in the ADF program package,[38] employing the hybrid PBE0 exchange-correlation functional[60] together with scalar relativistic corrections using the ZORA formalism[61] and all-electron Slater-type orbital functions, by using the triple-zeta plus polarization TZ2P+ and TZP basis sets for Ce and the other elements, respectively.[62] The amidinate ligand and $[Ce^{IV}\{PhC(N^tBu)_2\}_3]^+$ complex were optimized using restricted self-consistent field (SCF) approaches consistent with their closed-shell electronic configuration, whereas $[Ce^{III}\{PhC(N^tBu)_2\}_3]$ was calculated using an unrestricted spin-polarized SCF procedure with a spin multiplicity of two (doublet). The molecular symmetry was constrained to the $D_3$ point group for $[Ce^{III}\{PhC(N^tBu)_2\}_3]$ and $[Ce^{IV}\{PhC(N^tBu)_2\}_3]^+$ during the geometry optimizations. For the ligand, the symmetry was constrained to $C_2$. The resulting electronic structures were checked to ensure the absence of fractional or non-Aufbau orbital occupations. In the geometry optimization, the standard gradient algorithm was employed with two times tighter convergence criteria than the default ADF values.[38] To verify that the optimized structures correspond to minima on the potential energy surface, additional geometry optimizations were carried out at the PBE level of theory, followed by analytical vibrational frequency calculations. This approach was adopted because analytical second derivatives are available for PBE in ADF,[38] whereas frequency calculations at the hybrid PBE0 level require numerical differentiation and become computationally demanding for molecular systems of this size. The PBE frequency analyses confirmed the absence of imaginary modes, indicating that the optimized structures correspond to stable minima in the potential energy surface.

Electronic structures of both complexes were calculated by using DFT via the ADF code.[38] The hybrid PBE0 functional, scalar ZORA relativistic effect was used in the calculations. Optimized geometries as described above were utilized as input. The results were analyzed through molecular orbital diagrams (Figure 11) and total and partial density of states (DOS and PDOS) (Figure 6).

Ce $L_3$-edge XANES and VB-RIXS of $[Ce^{III}\{PhC(N^tBu)_2\}_3]$ were modelled using time-dependent DFT (TDDFT) via the ADF program package.[38] TDDFT allows us to simultaneously acquire explicit treatment of core-to-valence ($2p_{3/2} \rightarrow 5d$) transitions, and to evaluate the transition dipole moment (TDM) matrix elements necessary for both XANES and VB-RIXS modelling. Calculations were performed by using the PBE0 DFT functional at the spin-orbit level of theory.[58] The optimized structures obtained with the PBE0 DFT functional were used for the calculations. By including the spin-orbit coupling, the Kohn-Sham orbitals are treated as spinors and core and valence shells are split according to total angular momentum, which results in a separation of the lanthanide *2p* core shell into the twofold degenerate $2p_{1/2}$ and fourfold degenerate $2p_{3/2}$ spinor manifolds. Only the $2p_{3/2}$ core level was considered in the excitation space.

For the Ce $L_3$-edge XANES calculation, excitation energies and TDM associated with the ground state (GS, Ce $4f^1$), and intermediate state (IS Ce $2p_{3/2}^3 4f^1 5d^1$) were obtained using a single-particle method based on Kohn-Sham spinors. The average-of-configuration (AOC) type calculations was used.[44] Here, open-shell electrons were evenly distributed across the core $2p_{3/2}$ and valence *4f* and the *5d* spinors by using fractional occupation numbers.[63] This allowed us to

preserve near spherical symmetry while avoiding artificial symmetry breaking, which may cause complications in response calculations.[64] As a consequence, multiplet splitting due to *4f-5d* coulomb interactions could not be resolved, and therefore the calculation does not reproduce fine multiplet structures. For the GS electronic structure, 1 electron was evenly distributed over the fourteen-fold $4f_{5/2}$ + $4f_{7/2}$ spinors. For the IS, 3 electrons were distruvuted over the fourfold $2p_{3/2}$ spinors, 1 electron over the $4f_{5/2}$ + $4f_{7/2}$ spinors and 1 additional electron within the ten-fold $5d_{3/2}$ + $5d_{5/2}$ spinors. The ADF keyword "SelectExcitation" was used to generate the excited sates by defining an active space of Kohn-Sham spinors and the resulting manifold was restricted with the "UseOccupied" and "UseVirtual" keywords.[38] The "UseOccupied" space included the $2p_{3/2}$ core shell, and the "UseVirtual" spaced included the 5*d* spinors. In order to generate the Ce $L_3$-edge spectrum, the calculated oscillator strengths were broadened with Lorentzian function with half-width at half maximum (HWHM) parameter of 0.8 eV to simulate the finite core-hole lifetime broadening effects.

For the Ce $L_3$-edge VB-RIXS calculation, we also used TDDFT and the ADF program package.[38] A single-particle method based on Kohn-Sham spinors were used to obtain excitation energies and TDM associated with the ground state (GS, $4f^1$), intermediate state (IS, $2p_{3/2}^3 4f^1 5d^1$), and final state (FS, $5s_{1/2}^1 4f^1 5d^1$ and $4f^1 5d^1\underline{L}$) of the VB-RIXS process. Here, $\underline{L}$ signifies a valence exciton formed by excitation from predominantly ligand-based occupied spinors with sizeable Ce *5d* characters, which results in excited states with mixed ligand/*5d* character. Compared to the XANES calculations, an additional manifold representing the intermediate state was included as a logical result of the VB-RIXS process. To approximate the relevant electronic configurations, the AOC type calculations were used.[44] "UseOccupied" included the Ce $2p_{3/2}$ core shell, the Ce $5s_{1/2}$ semi-core orbitals (to account for high-energy transfer decay channels), and occupied valence spinors dominated by ligand character with larger-than-zero Ce 5*d* participation. The "UseVirtual" active space was restricted to the Ce *5d* valence orbitals only, which enforced an electron excitation in which all transitions reflected the VB-RIXS process at a lower computational cost, while excluding superfluous excitations into unrelated virtual states. The Kramers-Heisenberg formalism was used to compute VB-RIXS intensities,[65] which requires an explicit evaluation of the TDMs of the GS→IS and IS→FS processes. The "ESESTDM" keyword in ADF was used to obtain the excited-state-to-excited-state TDMs. A Lorentzian function was applied to both IS (HWHM 0.8 eV) and FS (HWHM 0.4 eV) within the Kramers-Heisenberg formula to simulate lifetime broadening effects.[65]

**Bond analysis.** QTAIM analysis was performed with DFT using the PBE0 DFT functional. The electron density ρ, potential V, and the delocalization index δ metrics were reported. Natural localized molecular orbital (NLMO) analyses were also with DFT (PBE0 functional). The method is based on natural bond order (NBO) formalism, which transforms the canonical Kohn-Sham orbitals into as set of localized ones that best describe Lewis-type electron pairs, lone pairs and delocalized interactions within two atoms. NLMOs corresponding to the Ce-N interactions were identified. And projection of each NKMOs in terms of atomic orbital contributions and the occupancy of the bonding orbitals were reported.

## ASSOCIATED CONTENT

The supporting information contains supplementary experimental (Synthesis, NMR, IR, Raman, XRD, ESI-MS, CV, HR-XANES, VB-RIXS, XAS, FDMNES) and theoretical results (Geometry Optimization, Electronic Structure).
This material is available free of charge via the Internet at [redacted]
Data files associated with figures provided in this manuscript and the supporting information is freely available in the Karlsruhe Institute of Technology's online data repository, KITOpen under the DOI 10.35097/yz910rbrssbsasjb.[66]

## AUTHOR INFORMATION

### Corresponding Author

* Tonya Vitova: tonya.vitova@kit.edu
Peter W. Roesky: peter.roesky@kit.edu
Lothar Weinhardt: lothar.weinhardt@kit.edu

### Author Contributions

The manuscript was written through contributions of all authors. All authors have given approval to the final version of the manuscript.

### Funding Sources

Deutsche Forschungsgemeinschaft (DFG) through the Collaborative Research Centre 4f for Future project A1 (CRC 1573, project number 471424360).

## ACKNOWLEDGMENT

The authors gratefully acknowledge the funding from the Deutsche Forschungsgemeinschaft (DFG, German Research Foundation) through the Collaborative Research Centre "4 f for Future" projects A1 (CRC 1573, project number 471424360). H.R. acknowledges the state of Baden-Württemberg for providing high-performance computing (HPC) support, time and infrastructure (BWunicluster). The authors thank the Institute for Beam Physics and Technology (IBPT) for the operation of the storage ring, the Karlsruhe Research Accelerator (KARA). D.H., L.W., and C.H. thank the DFG for funding in projects GZ:INST 121384/64-1 FUGG, GZ:INST 121384/65-1 FUGG, and GZ:INST 121384/66-1 FUGG.

## REFERENCES

(1) Lewis, G. N. The Atom and the Molecule. *J. Am. Chem. Soc.* **1916**, *38* (4), 762-785.
(2) Riedel, E.; Janiak, C. *Anorganische Chemie*; De Gruyter, 2022.
(3) Weber, B. Bond Theories. In *Coordination Chemistry: Basics and Current Trends*, Weber, B. Ed.; Springer Berlin Heidelberg, 2023; pp 47-72.
(4) Neidig, M. L.; Clark, D. L.; Martin, R. L. Covalency in f-Element Complexes. *Coord. Chem. Rev.* **2013**, *257* (2), 394-406.
(5) Vitova, T.; Roesky, P. W.; Dehnen, S. Open Questions on Bonding Involving Lanthanide Atoms. *Commun. Chem.* **2022**, *5* (1), 12.
(6) Balaram, V. Rare Earth Elements: A Review of Applications, Occurrence, Exploration, Analysis, Recycling, and Environmental Impact. *Geosci. Front.* **2019**, *10* (4), 1285-1303. Li, S.; Younis, A.; Chu, D. Cerium Oxide Nanostructures and their Applications. In *Functionalized Nanomaterials*, Farrukh, M. A. Ed.; IntechOpen, 2016.

(7) Branson, J. A.; Smith, P. W.; Sergentu, D.-C.; Russo, D. R.; Gupta, H.; Booth, C. H.; Arnold, J.; Schelter, E. J.; Autschbach, J.; Minasian, S. G. The Counterintuitive Relationship between Orbital Energy, Orbital Overlap, and Bond Covalency in $CeF_6^{2-}$ and $CeCl_6^{2-}$. *J. Am. Chem. Soc.* **2024**, *146* (37), 25640-25655.
(8) Minasian, S. G.; Batista, E. R.; Booth, C. H.; Clark, D. L.; Keith, J. M.; Kozimor, S. A.; Lukens, W. W.; Martin, R. L.; Shuh, D. K.; Stieber, S. C. E.; et al. Quantitative Evidence for Lanthanide-Oxygen Orbital Mixing in $CeO_2$, $PrO_2$, and $TbO_2$. *J. Am. Chem. Soc.* **2017**, *139* (49), 18052-18064.
(9) Cheisson, T.; Kersey, K. D.; Mahieu, N.; McSkimming, A.; Gau, M. R.; Carroll, P. J.; Schelter, E. J. Multiple Bonding in Lanthanides and Actinides: Direct Comparison of Covalency in Thorium(IV)- and Cerium(IV)-Imido Complexes. *J. Am. Chem. Soc.* **2019**, *141* (23), 9185-9190. Kaindl, G.; Kalkowski, G.; Brewer, W. D.; Sampathkumaran, E. V.; Holtzberg, F.; v. Wittenau, A. S. 4f Occupation and Hybridization from M-Shell Excitations in Rare-Earth Materials. *J. Magn. Magn. Mater.* **1985**, *47-48*, 181-189.
(10) Qiao, Y.; Yin, H.; Moreau, L. M.; Feng, R.; Higgins, R. F.; Manor, B. C.; Carroll, P. J.; Booth, C. H.; Autschbach, J.; Schelter, E. J. Cerium(IV) Complexes with Guanidinate Ligands: Intense Colors and Anomalous Electronic Structures. *Chem. Sci.* **2021**, *12* (10), 3558-3567, 10.1039/D0SC05193D.
(11) Vitova, T.; Ramanantoanina, H.; Schacherl, B.; Münzfeld, L.; Hauser, A.; Ekanayake, R. S. K.; Reitz, C. Y.; Prüßmann, T.; Neill, T. S.; Göttlicher, J.; et al. Photon-Modulated Bond Covalency of $[Sm(II)(\eta^9\text{-}C_9H_9)_2]$. *J. Am. Chem. Soc.* **2024**, *146* (30), 20577-20583.
(12) Ramanantoanina, H.; Rienmüller, J.; Lohse, Y. R.; Rauwolf, N.; Kehry, M.; Reitz, C.; Reynolds, E. M.; Prüßmann, T.; Schacherl, B.; Saveleva, V. A.; et al. Molecular-Metallic Binding Characteristics of the Intermetalloid f-/p-Block Cluster $[(La@In_2Bi_{11})_2Bi_2]^{6-}$. *Angew. Chem., Int. Ed.* **2025**, e202512019. Afshani, J.; Delgado, T.; Rosspeintner, A.; Hagemann, H. Luminescence Spectroscopy of Anomalous $Eu^{3+}$ in Ternary Aluminates: Experimental Evidence for Covalent Bonding of 4f-Orbitals of Lanthanides. *J. Lumin.* **2023**, *263*, 120043. Chen, Y.-M.; Wang, C.-Z.; Wu, Q.-Y.; Lan, J.-H.; Chai, Z.-F.; Nie, C.-M.; Shi, W.-Q. Complexation of Trivalent Lanthanides and Actinides with Diethylenetriaminepentaacetic Acid: Theoretical Unraveling of Bond Covalency. *J. Mol. Liq.* **2020**, *299*, 112174.
(13) Ramanantoanina, H.; Schacherl, B.; Kovács, A.; Tagliavini, M.; Reynolds, E. M.; Reitz, C.; Ekanayake, R. S. K.; Schäfer, M.; von Massow, P.-V.; Göttlicher, J.; et al. High-Energy Resolution X-Ray Spectroscopy Reveals Long-Sought Bonding Characteristics of $La^{3+}$ Homologues for Radiopharmaceuticals. *Commun. Chem.* **2026**.
(14) Willauer, A. R.; Palumbo, C. T.; Scopelliti, R.; Zivkovic, I.; Douair, I.; Maron, L.; Mazzanti, M. Stabilization of the Oxidation State +IV in Siloxide-Supported Terbium Compounds. *Angew. Chem., Int. Ed.* **2020**, *59* (9), 3549-3553.
(15) Boggiano, A. C.; Studvick, C. M.; Roy Chowdhury, S.; Niklas, J. E.; Tateyama, H.; Wu, H.; Leisen, J. E.; Kleemiss, F.; Vlaisavljevich, B.; Popov, I. A.; La Pierre, H. S. Praseodymium in the Formal +5 Oxidation State. *Nat. Chem.* **2025**, *17* (7), 1005-1010.
(16) Kerridge, A. Quantification of f-Element Covalency Through Analysis of the Electron Density: Insights From Simulation. *Chem. Commun.* **2017**, *53* (50), 6685-6695. Su, J.; Batista, E. R.; Boland, K. S.; Bone, S. E.; Bradley, J. A.; Cary, S. K.; Clark, D. L.; Conradson, S. D.; Ditter, A. S.; Kaltsoyannis, N.; et al. Energy-Degeneracy-Driven Covalency in Actinide Bonding. *J. Am. Chem. Soc.* **2018**, *140* (51), 17977-17984.
(17) Sergentu, D.-C.; Booth, C. H.; Autschbach, J. Probing Multiconfigurational States by Spectroscopy: The Cerium XAS $L_3$-Edge Puzzle. *Chem. - Eur. J* **2021**, *27* (25), 7239-7251.
(18) Smiles, D. E.; Batista, E. R.; Booth, C. H.; Clark, D. L.; Keith, J. M.; Kozimor, S. A.; Martin, R. L.; Minasian, S. G.; Shuh, D. K.; Stieber, S. C. E.; Tyliszczak, T. The duality of electron localization and covalency in lanthanide and actinide metallocenes. *Chemical Science* **2020**, *11* (10), 2796-2809, 10.1039/C9SC06114B.
(19) Walter, M. D.; Booth, C. H.; Lukens, W. W.; Andersen, R. A. Cerocene Revisited: The Electronic Structure of and Interconversion Between $Ce_2(C_8H_8)_3$ and $Ce(C_8H_8)_2$. *Organometallics* **2009**, *28* (3), 698-707.
(20) Edelstein, N. M.; Allen, P. G.; Bucher, J. J.; Shuh, D. K.; Sofield, C. D.; Kaltsoyannis, N.; Maunder, G. H.; Russo, M. R.; Sella, A. The Oxidation State of Ce in the Sandwich Molecule Cerocene. *J. Am. Chem. Soc.* **1996**, *118* (51), 13115-13116.
(21) Dolg, M.; Fulde, P.; Stoll, H.; Preuss, H.; Chang, A.; Pitzer, R. M. Formally Tetravalent Cerium and Thorium Compounds: a Configuration Interaction Study of Cerocene $Ce(C_8H_8)_2$ and Thorocene $Th(C_8H_8)_2$ Using Energy-Adjusted Quasirelativistic Ab Initio Pseudopotentials. *Chem. Phys.* **1995**, *195* (1), 71-82.
(22) Pauling, L. *General Chemistry*; Dover Publications, 1988.
(23) Ashley, A.; Balazs, G.; Cowley, A.; Green, J.; Booth, C. H.; O'Hare, D. Bis(permethylpentalene)cerium – Another Ambiguity in Lanthanide Oxidation State. *Chem. Commun.* **2007**, (15), 1515-1517.
(24) Booth, C. H.; Walter, M. D.; Daniel, M.; Lukens, W. W.; Andersen, R. A. Self-Contained Kondo Effect in Single Molecules. *Phys. Rev. Lett.* **2005**, *95* (26), 267202.
(25) Moreau, L. M.; Lapsheva, E.; Amaro-Estrada, J. I.; Gau, M. R.; Carroll, P. J.; Manor, B. C.; Qiao, Y.; Yang, Q.; Lukens, W. W.; Sokaras, D.; et al. Electronic Structure Studies Reveal 4f/5d Mixing and its Effect on Bonding Characteristics in Ce-Imido and -Oxo Complexes. *Chem. Sci.* **2022**, *13* (6), 1759-1773.
(26) Halbach, R. L.; Nocton, G.; Booth, C. H.; Maron, L.; Andersen, R. A. Cerium Tetrakis(tropolonate) and Cerium Tetrakis(acetylacetonate) Are Not Diamagnetic but Temperature-Independent Paramagnets. *Inorg. Chem.* **2018**, *57* (12), 7290-7298. Rice, N. T.; Popov, I. A.; Russo, D. R.; Gompa, T. P.; Ramanathan, A.; Bacsa, J.; Batista, E. R.; Yang, P.; La Pierre, H. S. Comparison of Tetravalent Cerium and Terbium Ions in a Conserved, Homoleptic Imidophosphorane Ligand Field. *Chem. Sci.* **2020**, *11* (24), 6149-6159. Tateyama, H.; Liao, C.; Wilkinson, G. R.; Ramanathan, A.; Amidani, L.; Bazarkina, E.; Ressnik, F.; Engle, K. S.; Bacsa, J.; Sokaras, D.; et al. Single-Determinant Ground State in $Ce^{4+}$ Imidophosphorane Complexes. *Inorg. Chem.* **2025**. Wilson, H. H.; Yu, X.; Cheisson, T.; Smith, P. W.; Pandey, P.; Carroll, P. J.; Minasian, S. G.; Autschbach, J.; Schelter, E. J. Synthesis and Characterization of a Bridging Cerium(IV) Nitride Complex. *J. Am. Chem. Soc.* **2023**, *145* (2), 781-786.
(27) Dröse, P.; Hrib, C. G.; Edelmann, F. T. Synthesis and Structural Characterization of a Homoleptic Cerium(III) Propiolamidinate. *J. Organomet. Chem.* **2010**, *695* (17), 1953-1956. Kloditz, R.; Fichter, S.; Kaufmann, S.; Brunner, T. S.; Kaden, P.; Patzschke, M.; Stumpf, T.; Roesky, P. W.; Schmidt, M.; März, J. Series of Tetravalent Actinide Amidinates: Structure Determination and Bonding Analysis. *Inorg. Chem.* **2020**, *59* (21), 15670-15680. Werner, D.; Deacon, G. B.; Junk, P. C.; Anwander, R. Cerium(III/IV) Formamidinate Chemistry, and a Stable Cerium(IV) Diolate. *Chem. - Eur. J* **2014**, *20* (15), 4426-4438.
(28) Scott, N. M.; Dorta, R.; Stevens, E. D.; Correa, A.; Cavallo, L.; Nolan, S. P. Interaction of a Bulky N-Heterocyclic Carbene Ligand with Rh(I) and Ir(I). Double C−H Activation and Isolation of Bare 14-Electron Rh(III) and Ir(III) Complexes. *J. Am. Chem. Soc.* **2005**, *127* (10), 3516-3526.
(29) Cendrowski-Guillaume, S. M.; Nierlich, M.; Lance, M.; Ephritikhine, M. First Chemical Transformations of Lanthanide Borohydride Compounds: Synthesis and Crystal Structures of [(η-C8H8)Nd(BH4)(THF)]2 and [(η-C8H8)Nd(THF)4][BPh4]. *Organometallics* **1998**, *17* (5), 786-788.
(30) Krossing, I. The Facile Preparation of Weakly Coordinating Anions: Structure and Characterisation of Silverpolyfluoroalkoxyaluminates AgAl(ORF)4, Calculation of the Alkoxide Ion Affinity. *Chem. - Eur. J* **2001**, *7* (2), 490-502.
(31) Shannon, R. D. Revised effective ionic radii and systematic studies of interatomic distances in halides and chalcogenides. *Foundations of Crystallography* **1976**, *32* (5), 751-767.

(32) Shannon, R. Revised Effective Ionic Radii and Systematic Studies of Interatomic Distances in Halides and Chalcogenides. *Acta Crystallogr., Sect. A* **1976**, *32* (5), 751-767.
(33) Bianconi, A.; Marcelli, A.; Dexpert, H.; Karnatak, R.; Kotani, A.; Jo, T.; Petiau, J. Specific Intermediate-Valence State of Insulating 4f Compounds Detected by $L_3$ X-Ray Absorption. *Phys. Rev. B* **1987**, *35* (2), 806-812.
(34) Kvashnina, K. O. Electronic-Structure Interpretation: How Much Do We Understand Ce $L_3$ XANES? *Chem. - Eur. J* **2024**, *30* (46), e202400755.
(35) Kotani, A. Core-Hole Effect in the Ce $L_3$ X-Ray Absorption Spectra of $CeO_2$ and $CeFe_2$: New Examination by Using Resonant X-Ray Emission Spectroscopy. *Mod. Phys. Lett. B* **2013**, *27* (16), 1330012. Soldatov, A. V.; Ivanchenko, T. S.; Della Longa, S.; Kotani, A.; Iwamoto, Y.; Bianconi, A. Crystal-Structure Effects in the Ce $L_3$-Edge X-Ray-Absorption Spectrum of $CeO_2$: Multiple-Scattering Resonances and Many-Body Final States. *Phys. Rev. B* **1994**, *50* (8), 5074-5080.
(36) Pruessmann, T.; Nagel, P.; Simonelli, L.; Batchelor, D.; Gordon, R.; Schimmelpfennig, B.; Trumm, M.; Vitova, T. Opportunities and Challenges of Applying Advanced X-Ray Spectroscopy to Actinide and Lanthanide N-Donor Ligand Systems. *J. Synchrotron Radiat.* **2022**, *29* (1), 53-66.
(37) Materials Data on $CeO_2$ by Materials Project. LBNL Materials Project; Lawrence Berkeley National Laboratory (LBNL), Berkeley, CA (United States): United States, 2020.
(38) Baerends, E. J.; Aguirre, N. F.; Austin, N. D.; Autschbach, J.; Bickelhaupt, F. M.; Bulo, R.; Cappelli, C.; van Duin, A. C. T.; Egidi, F.; Fonseca Guerra, C.; et al. The Amsterdam Modeling Suite. *J. Chem. Phys.* **2025**, *162* (16).
(39) Wojdyr, M. Fityk: A General-Purpose Peak Fitting Program. *J. Appl. Crystallogr.* **2010**, *43* (5 Part 1), 1126-1128.
(40) de Groot, F. M. F.; Elnaggar, H.; Frati, F.; Wang, R.-p.; Delgado-Jaime, M. U.; van Veenendaal, M.; Fernandez-Rodriguez, J.; Haverkort, M. W.; Green, R. J.; van der Laan, G.; et al. 2p x-ray absorption spectroscopy of 3d transition metal systems. *J. Electron Spectrosc. Relat. Phenom.* **2021**, *249*, 147061.
(41) Kotani, A.; Kvashnina, K. O.; Butorin, S. M.; Glatzel, P. Spectator and Participator Processes in the Resonant Photon-In and Photon-Out Spectra at the Ce $L_3$ Edge of $CeO_2$. *The European Physical Journal B* **2012**, *85* (8), 257.
(42) Ramanantoanina, H. LFDFT—A Practical Tool for Coordination Chemistry. *Computation* **2022**, *10* (5), 70.
(43) Bondino, F.; Magnano, E.; Booth, C. H.; Offi, F.; Panaccione, G.; Malvestuto, M.; Paolicelli, G.; Simonelli, L.; Parmigiani, F.; McGuire, M. A.; et al. Electronic Structure of $CeFeAsO_{1-x}F_x$ (x=0, 0.11, and 0.12). *Phys. Rev. B* **2010**, *82* (1), 014529.
(44) Ramanantoanina, H. A DFT-Based Theoretical Model for the Calculation of Spectral Profiles of Lanthanide $M_{4,5}$-Edge X-Ray Absorption. *J. Chem. Phys.* **2018**, *149* (5).
(45) Yagci, O. The M4,5 photo-absorption spectra of cerium in CeO2 and oxidation of metallic cerium. *Journal of Physics C: Solid State Physics* **1986**, *19* (18), 3487.
(46) Paidi, V. K.; Brewe, D. L.; Freeland, J. W.; Roberts, C. A.; van Lierop, J. Role of Ce *4f* hybridization in the origin of magnetism in nanoceria. *Phys. Rev. B* **2019**, *99* (18), 180403.
(47) Reed, A. E.; Weinhold, F. Natural Localized Molecular Orbitals. *J. Chem. Phys.* **1985**, *83* (4), 1736-1740.
(48) Bader, R. F. W. *Atoms in Molecules: A Quantum Theory*; Oxford University Press, 1990.
(49) Solé, V. A.; Papillon, E.; Cotte, M.; Walter, P.; Susini, J. A Multiplatform Code for the Analysis of Energy-Dispersive X-Ray Fluorescence Spectra. *Spectrochim. Acta, Part B* **2007**, *62* (1), 63-68.
(50) Schacherl, B.; Tagliavini, M.; Kaufmann-Heimeshoff, H.; Göttlicher, J.; Mazzanti, M.; Popa, K.; Walter, O.; Pruessmann, T.; Vollmer, C.; Beck, A.; et al. Resonant Inelastic X-ray Scattering Tools to Count 5 f Electrons of Actinides and Probe Bond Covalency. *Nat. Commun.* **2025**, *16* (1), 1221.
(51) Schacherl, B.; Prüssmann, T.; Dardenne, K.; Hardock, K.; Krepper, V.; Rothe, J.; Vitova, T.; Geckeis, H. Implementation of Cryogenic Tender X-ray HR-XANES Spectroscopy at the ACT Station of the CAT-ACT Beamline at the KIT Light Source. *J. Synchrotron Radiat.* **2022**, *29* (Pt 1), 80-88.
(52) Ravel, B.; Newville, M. ATHENA, ARTEMIS, HEPHAESTUS: Data Analysis for X-ray Absorption Spectroscopy Using IFEFFIT. *J. Synchrotron Radiat.* **2005**, *12* (4), 537-541.
(53) *OriginPro*; OriginLab Corporation,: 2025. (accessed 2025).
(54) Weinhardt, L.; Steininger, R.; Kreikemeyer-Lorenzo, D.; Mangold, S.; Hauschild, D.; Batchelor, D.; Spangenberg, T.; Heske, C. X-SPEC: a 70 eV to 15 keV Undulator Beamline for X-Ray and Electron Spectroscopies. *J. Synchrotron Radiat.* **2021**, *28* (2), 609-617.
(55) Weinhardt, L.; Wansorra, C.; Steininger, R.; Spangenberg, T.; Hauschild, D.; Heske, C. High-Transmission Spectrometer for Rapid Resonant Inelastic Soft X-Ray Scattering (rRIXS) Maps. *J. Synchrotron Radiat.* **2024**, *31* (6), 1481-1488.
(56) Perdew, J. P.; Burke, K.; Ernzerhof, M. Generalized Gradient Approximation Made Simple. *Phys. Rev. Lett.* **1996**, *77* (18), 3865-3868.
(57) Ernzerhof, M.; Scuseria, G. E. Assessment of the Perdew–Burke–Ernzerhof Exchange-Correlation Functional. *J. Chem. Phys.* **1999**, *110* (11), 5029-5036.
(58) van Lenthe, E.; Baerends, E. J.; Snijders, J. G. Relativistic Total Energy Using Regular Approximations. *J. Chem. Phys.* **1994**, *101* (11), 9783-9792.
(59) Grimme, S.; Antony, J.; Ehrlich, S.; Krieg, H. A Consistent and Accurate Ab Initio Parametrization of Density Functional Dispersion Correction (DFT-D) for the 94 Elements H-Pu. *J. Chem. Phys.* **2010**, *132* (15), 154104.
(60) Adamo, C.; Barone, V. Toward Reliable Density Functional Methods Without Adjustable Parameters: The PBE0 Model. *J. Chem. Phys.* **1999**, *110* (13), 6158-6170.
(61) Lenthe, E. v.; Baerends, E. J.; Snijders, J. G. Relativistic Regular Two-Component Hamiltonians. *J. Chem. Phys.* **1993**, *99* (6), 4597-4610.
(62) Van Lenthe, E.; Baerends, E. J. Optimized Slater-Type Basis Sets for the Elements 1–118. *J. Comput. Chem.* **2003**, *24* (9), 1142-1156.
(63) Ramanantoanina, H.; Sahnoun, M.; Barbiero, A.; Ferbinteanu, M.; Cimpoesu, F. Development and Applications of the LFDFT: the Non-Empirical Account of Ligand Field and the Simulation of the f–d Transitions by Density Functional Theory. *Phys. Chem. Chem. Phys.* **2015**, *17* (28), 18547-18557, 10.1039/C5CP02349A.
(64) Cordova, F.; Doriol, L. J.; Ipatov, A.; Casida, M. E.; Filippi, C.; Vela, A. Troubleshooting Time-Dependent Density-Functional Theory for Photochemical Applications: Oxirane. *J. Chem. Phys.* **2007**, *127* (16).
(65) Neill, T. S.; Ramanantoanina, H.; Palina, N.; Prüßmann, T.; Rothe, J.; Gaona, X.; Fellhauer, D.; Schild, D.; Wansorra, C.; Hauschild, D.; et al. The Role of Halides in the Bonding and Electronic Structure of Actinyl(VI) Halides—Energy Match Driven Stability. *J. Am. Chem. Soc.* **2025**, *147* (39), 35401-35412.
(66) Reynolds, E. M.; Günther-Schmidt, N.; Steininger, R.; Reitz, C. Y.; Göttlicher, J.; Wansorra, C.; Blankenship, M.; Branson, J. A.; Sun, X.; Schacherl, B.; et al. Data for "How the Oxidation State Drives Bonding Properties in $Ce^{III}$ and $Ce^{IV}$ Tris(amidinate) Complexes. Karlsruhe Institute for Technology: KITOpen, 2026.